JGR Solid Earth

RESEARCH ARTICLE
10.1029/2024JB030926

The 2021 M_W 8.1 Kermadec Earthquake Sequence: Great Earthquake Rupture Along the Mantle/Slab Contact

Lingling Ye[1], Yangming Hu[1], Tao Xia[1], Thorne Lay[2], Yingquan Sang[1,3], Xiaofei Chen[1], Hiroo Kanamori[4], Fabrizio Romano[5], Stefano Lorito[5], and Zhou Gui[6]

[1]Department of Earth and Space Sciences, Southern University of Science and Technology, Shenzhen, China, [2]Department of Earth and Planetary Sciences, University of California Santa Cruz, Santa Cruz, CA, USA, [3]Institute of Geology and Geophysics, Chinese Academy of Sciences, Beijing, China, [4]Seismological Laboratory, California Institute of Technology, Pasadena, CA, USA, [5]Istituto Nazionale di Geofisica e Vulcanologia, Roma, Italy, [6]Institute of Oceanology Chinese Academy of Sciences, Qingdao, China

Abstract Most great earthquakes on subduction zone plate boundaries have large coseismic slip concentrated along the contact between the subducting slab and the upper plate crust. On 4 March 2021, a magnitude 7.4 foreshock struck 1 hr 47 min before a magnitude 8.1 earthquake along the northern Kermadec island arc. The mainshock is the largest well-documented underthrusting event along the ~2,500-km long Tonga-Kermadec subduction zone. Using teleseismic, geodetic, and tsunami data, we find that all substantial coseismic slip in the mainshock is located along the mantle/slab interface at depths from 20 to 55 km, with the large foreshock nucleating near the down-dip edge. Smaller foreshocks and most aftershocks are located up-dip of the mainshock, where substantial prior moderate thrust earthquake activity had occurred. The upper plate crust is ~17 km thick in northern Kermadec with only moderate-size events along the crust/slab interface. A 1976 sequence with M_W values of 7.9, 7.8, 7.3, 7.0, and 7.0 that spanned the 2021 rupture zone also involved deep megathrust rupture along the mantle/slab contact, but distinct waveforms exclude repeating ruptures. Variable waveforms for eight deep M6.9+ thrusting earthquakes since 1990 suggest discrete slip patches distributed throughout the region. The ~300-km long plate boundary in northern Kermadec is the only documented subduction zone region where the largest modeled interplate earthquakes have ruptured along the mantle/slab interface, suggesting that local frictional properties of the putatively hydrated mantle wedge may involve a dense distribution of Antigorite-rich patches with high slip rate velocity weakening behavior in this locale.

Plain Language Summary On 4 March 2021, a magnitude 8.1 earthquake struck northern Kermadec, the largest well-documented thrust event along the Tonga-Kermadec boundary. It was preceded by a magnitude 7.4 foreshock 1 hr 47 min earlier. We find that all substantial slip is located at depths >20 km, with the foreshock nucleating down-dip of the mainshock. A moderate number of small events occurred between the two events, mainly concentrated up-dip of the mainshock large-slip zone, where prior seismicity and most aftershocks are also located. The M8.1 mainshock is most notable for having all large coseismic slip lie along the mantle/slab contact, distinct from typical great subduction zone earthquakes with most rupture along the crust/slab contact. The ~300-km long portion of the plate boundary interface in northern Kermadec is the only documented region where the largest modeled interplate earthquakes have ruptured along the mantle/slab interface. A prior major sequence in 1976 overlaps the 2021 rupture zone, but the difference in seismic waveforms indicates heterogeneous interplate coupling. The occurrence of frequent large earthquakes on the mantle/slab interface and the temporal clusters of major ruptures in 1976 and 2021 requires unusual frictional properties, possibly with velocity weakening in a patchy distribution of serpentinite phases along the interface.

Key Points:

- The 2021 Kermadec plate boundary sequence with an M_W 7.4 foreshock and M_W 8.1 mainshock involved large slip at depths from 20 to 55 km
- Prior large thrust events in the region also appear to have ruptured similar depths, with smaller events located on the shallow megathrust
- The mantle/slab contact in northern Kermadec hosts frequent large earthquakes, indicating heterogeneous patchy velocity weakening friction

Supporting Information:

Supporting Information may be found in the online version of this article.

Correspondence to:

L. Ye,
yell@sustech.edu.cn

Citation:

Ye, L., Hu, Y., Xia, T., Lay, T., Sang, Y., Chen, X., et al. (2025). The 2021 M_W 8.1 Kermadec earthquake sequence: Great earthquake rupture along the mantle/slab contact. *Journal of Geophysical Research: Solid Earth*, *130*, e2024JB030926. https://doi.org/10.1029/2024JB030926

Received 11 DEC 2024
Accepted 24 MAR 2025

Author Contributions:

Conceptualization: Lingling Ye
Formal analysis: Lingling Ye, Yangming Hu, Tao Xia, Yingquan Sang, Fabrizio Romano
Funding acquisition: Lingling Ye, Thorne Lay, Xiaofei Chen
Investigation: Thorne Lay, Xiaofei Chen, Hiroo Kanamori, Fabrizio Romano, Stefano Lorito, Zhou Gui
Methodology: Lingling Ye
Writing – original draft: Lingling Ye
Writing – review & editing: Lingling Ye, Yangming Hu, Tao Xia, Thorne Lay, Yingquan Sang, Xiaofei Chen, Hiroo Kanamori, Fabrizio Romano, Stefano Lorito, Zhou Gui

1. Introduction

Great earthquakes, which have seismic magnitudes >8, are most commonly located on the shallow plate boundaries in subduction zones where oceanic plates underthrust overriding oceanic or continental plates (Figure 1). The depth range of the contact between the upper plate crust and underthrusting oceanic slab varies accordingly from <30 km for island arcs to 25–45 km for continental arcs (e.g., Laske et al., 2013; Szwillus et al., 2019). At greater depths in both island and continental arcs, the forearc mantle wedge is in contact with the slab surface, and silica-rich aqueous fluids released from the slab due to dehydration reactions can interact with

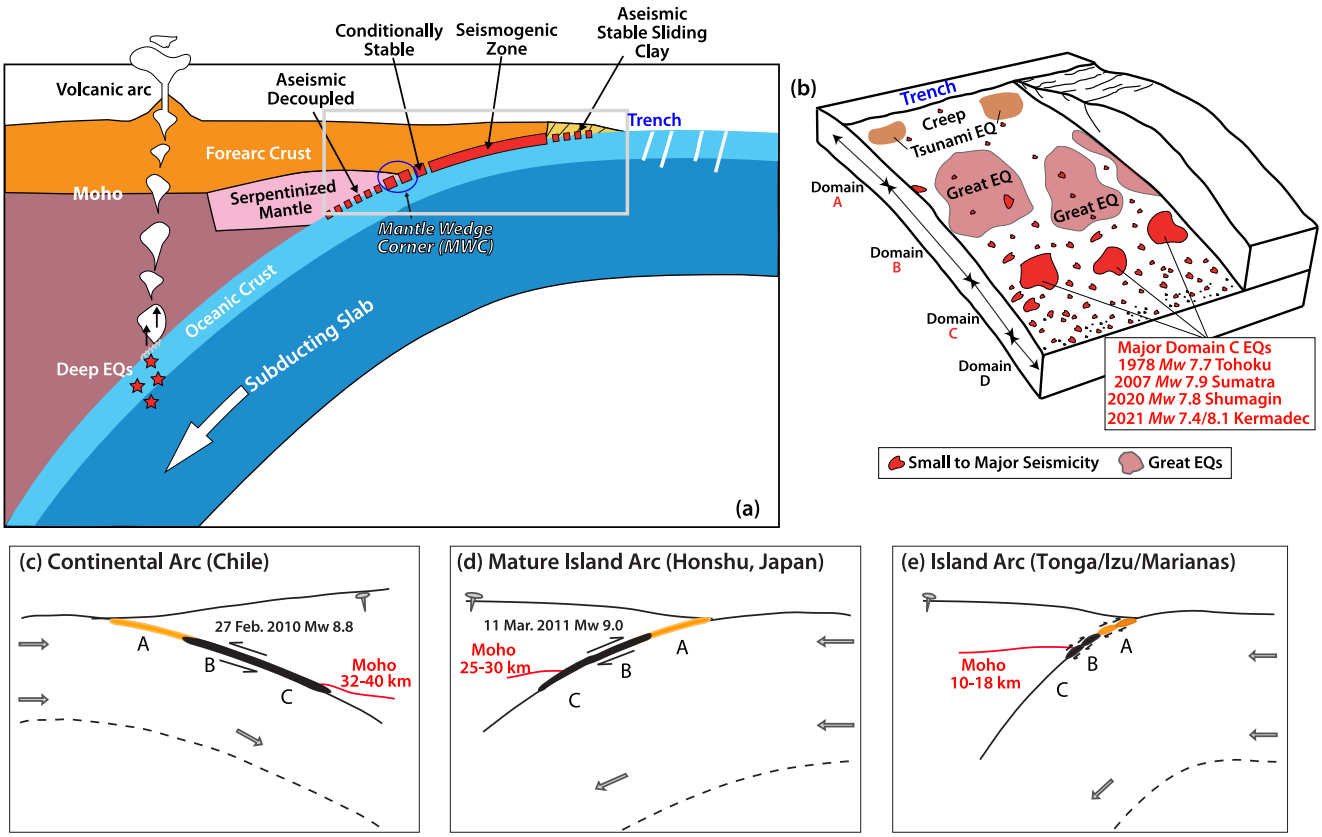

Figure 1. Schematic setting and rupture style in subduction zones. (a) Conceptual model for megathrust rupture and deep (>70 km) earthquakes modified from Oleskevich et al. (1999) and Gerya et al. (2006). (b) Schematic characterization of megathrust friction and rupture modified from Lay et al. (2012) and Ye, Lay, Kanamori, Yamazaki, and Cheung (2021), with Domains A–D corresponding to different depth ranges along the megathrust from the shallow trench to the downdip brittle-ductile transition. Small bright red, flat red, and brown patches indicate small to major seismicity, great earthquakes, and shallow tsunami earthquakes, respectively. Large domain C earthquakes are highlighted. (c–e) Schematic cross-sections of megathrust rupture with Moho depth for continental Arc (Chile), mature Island Arc (Honshu, Japan), and Island Arc in Tonga, Izu, and Marianas subduction zones, respectively. Labels A–C correspond to the Domains A–C in panel (b).

the forearc mantle material to produce hydrous minerals such as serpentine, talc and chlorite (e.g., Bostock et al., 2002; Blakely et al., 2005; Deschamps et al., 2013; Hyndman et al., 1997; Hyndman & Peacock, 2003; Moore et al., 1987; Moore & Lockner, 2007; Peacock, 1993; Peacock & Hyndman, 1999; Reynard, 2013; Wada & Wang, 2009; Figure 1) which usually exhibit a velocity-strengthening behavior. Previous research indicates that the mantle wedge corner is typically rich in weak hydrous minerals in relatively warm environments resulting in a downdip limit to megathrust ruptures. Serpentinization and temperature increase along the mantle/slab contact is expected to modify frictional behavior, abetting a progressive transition from velocity-weakening and stick-slip failures along the crust/slab contact to slow slip events and/or ductile deformation and melange development along the mantle/slab contact (e.g., Guillot et al., 2015; Hyndman, 2007; Wang et al., 2020, 2025).

Analyses of the coseismic slip distributions from great earthquakes on subduction megathrusts indicate that large-slip regions are primarily located along the crust/slab contact, with secondary extension along the mantle/slab contact for some great events, as in Figures 1c and 1d (e.g., Lay, 2018; Lay et al., 2012; Wang et al., 2020). A few deep major thrust earthquakes have ruptured mostly or entirely below the crust/slab contact beneath continental arcs or mature island arcs, such as the 1978 M_W 7.7 Miyagi-Oki, Japan, 2007 M_W 7.9 Kepulauan, Sumatra (Ye, Lay, Kanamori, Yamazaki, & Cheung, 2021), and 2007 M_W 7.7 Tocopilla, Chile (Chlieh et al., 2011; Delouis et al., 2009) events (Figure 1b). These earthquakes ruptured the deeper megathrust in regions of relatively thick upper plate crust where great events have occurred at shallower depths. The mantle wedge is relatively low temperature in these cases, but most island arcs will tend to be warmer at corresponding depths, and deep ruptures should be less common (Figure 1e). However, this study demonstrates that the northern Kermadec subduction zone is an unusual island arc with great earthquake occurrence deeper than the upper plate crust, involving an M_W

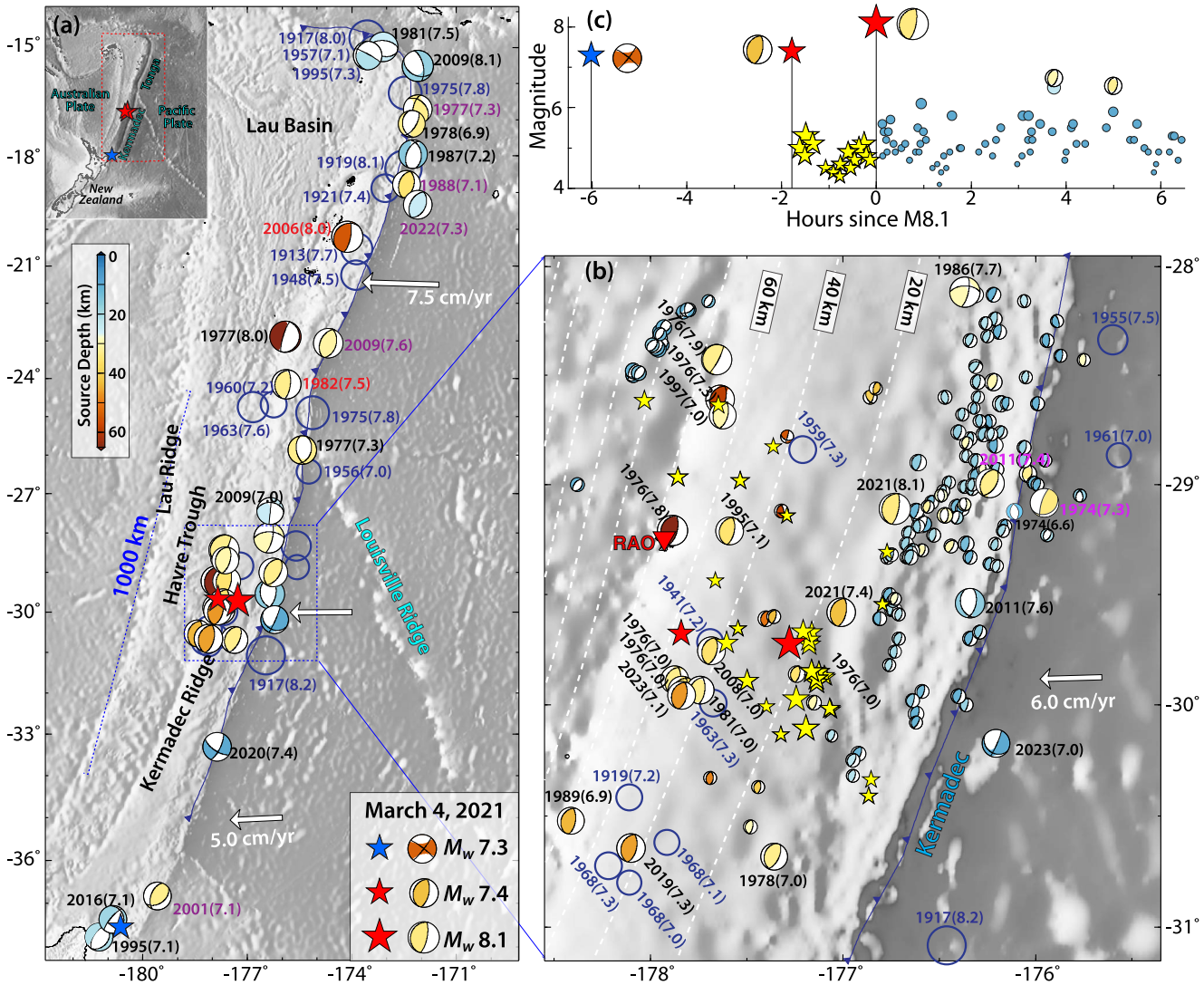

Figure 2. Major earthquakes along the Tonga-Kermadec subduction zone and the 2021 M_W 8.1 Kermadec sequence. (a) Major earthquakes since 1900: blue circles show M7+ earthquakes from the USGS-NEIC catalog from 1900 to 1975, and focal mechanisms show M6.9+ events from the GCMT catalog since 1976 color-coded with source centroid depths. Red stars indicate the epicentral locations of the M_W 7.4 and M_W 8.1 events on 4 March 2021. The inset map shows the large-scale plate tectonic setting with the Pacific plate underthrusting the Australian plate along the Tonga and Kermadec subduction zones. The white vectors indicate the relative motion of the Pacific plate for a fixed Australian plate. (b) Major earthquakes around the 2021 Kermadec sequence along with 60-day aftershocks (small focal mechanisms) from the GCMT catalog plotted at the USGS-NEIC epicentral locations (except for the M_W 7.4 and M_W 8.1 events, which are plotted at the GCMT centroid locations). The focal mechanism for the 1974 M_W 7.3 earthquake is from Chapple and Forsyth (1974). Yellow stars show epicenters of events between the M_W 7.4 and M_W 8.1 events (USGS-NEIC and ISC catalogs). (c) Time sequence of earthquake magnitudes in the 2021 sequence from the USGS-NEIC catalog. Yellow stars indicate the events between the M_W 7.4 and M_W 8.1 events, while blue circles are early aftershocks, along with GCMT mechanisms for large events.

8.1 thrust event on 4 March 2021. This provides a unique opportunity to explore the rupture mechanism on the mantle/slab contact.

2. Tectonic Setting of the 4 March 2021 Kermadec Sequence

The Tonga-Kermadec subduction zone extends from ~15°S to ~38°S with the convergence of the Pacific plate at the trench involving rates from 5 to 24 cm/yr (Bevis et al., 1995; DeMets et al., 2010; Pelletier & Louat, 1989). The Louisville Ridge on the incoming Pacific plate disrupts the convergence zone, separating the Kermadec and Tonga portions of the island arc, and produces local large interplate and intraplate earthquakes (e.g., Christensen & Lay, 1988; Eissler & Kanamori, 1982; Figures 2a and S1 in Supporting Information S1). There is reduced seismicity near 36°S, where the Hikurangi Plateau converges and delimits the southern Kermadec trench. The

northern Kermadec region (28°S–31.1°S) has hosted the largest recorded (M_W 7.5–8.2) earthquakes along the Kermadec subduction zone, and there is a secondary concentration of M_W 7.1–7.5 events at the southern end of the Kermadec arc from 37°S to 38°S, just northeast of the incoming Hikurangi Plateau (Figure 2a). Along the Kermadec subduction zone, back-arc basin spreading in the Havre Trough west of the Kermadec Ridge began about 5.5 million years ago and may still have slow active spreading (Tontini et al., 2019). A seismic reflection profile near 29°S indicates an upper plate with a buried Tonga Ridge in the forearc seaward of the Kermadec Ridge and an upper plate crustal thickness of ∼17 km (Bassett et al., 2016). The Tonga and Kermadec Ridges account for the thickened upper oceanic plate. The incoming Pacific plate age is >80 Ma (e.g., Müller et al., 2008), so a relatively low-temperature regime is expected along the shallow megathrust, but the recent back-arc spreading suggests significant deformation in the mantle wedge.

On 4 March 2021, an M_W 8.1 earthquake (19:28:33 UTC, 29.723°S, 177.279°W, hypocenter depth 28.9 km; U.S. Geological Survey National Earthquake Information Center (USGS-NEIC), https://earthquake.usgs.gov/earthquakes/eventpage/us7000dflf/executive) struck the northern Kermadec subduction zone, preceded by an M_W 7.4 foreshock (17:41:23 UTC, 29.677°S, 177.840°W, hypocenter depth 43.0 km; USGS-NEIC, https://earthquake.usgs.gov/earthquakes/eventpage/us7000dfk3/executive). The M_W 8.1 event is the largest recorded event known to be on the plate interface along the entire Tonga-Kermadec subduction zone. No local detectable anomalous seismicity preceded the large M_W 7.4 foreshock, but at least 15 small events occurred in the 1 hr 47 min between the two large earthquakes and there was extensive aftershock activity with some events exceeding magnitude 4.5 (Figure 2c). An M_W 7.3 event (13:27:34 UTC, 37.479°S, 179.458°W, 10.0 km deep; USGS-NEIC, https://earthquake.usgs.gov/earthquakes/eventpage/us7000dffl/executive) occurred within the slab in the active region just northeast of New Zealand 6 hrs before the northern Kermadec M_W 8.1 mainshock (Figures 2a and 2c). The distance between the events is ∼885 km, so any interaction is unclear.

Prior to the 2021 rupture, the interface had been inferred to be locked based on sustained interseismic westward ground velocity at GeoNet GNSS Station RAUL on Raoul Island (Figure 3a), installed in 2009 (Power et al., 2012; Wallace et al., 2009). The limited seismic record and uncertainty of source locations in early catalogs make it difficult to determine the recurrence time for large earthquakes in the northern Kermadec region from 28°S to 31.1°S (e.g., McCann et al., 1979). Historically, this region experienced very large events on 1 May 1917 (ISC-GEM Global Instrumental Earthquake Catalog: 31.080°S, 176.461°W, M_S 8.1, M_W 8.2) and 16 November 1917 (M_S 7.7); two interplate thrust events on 14 January 1976 with M_W 7.9 and M_W 7.8, along with M_W 7.3, 7.0 and 7.0 events; and an intraslab oblique rupture on 20 October 1986 with M_W 7.7 (Figure 2b; Houston et al., 1993; Lundgren et al., 1989). As discussed below, there is substantial uncertainty in the location and mechanism of the 1917 activity, but a first-order estimate of ∼60 years recurrence interval for large events in the region has been proposed (e.g., Lythgoe et al., 2023; Nishenko, 1991).

The northern Kermadec region has also experienced large near-trench intraplate faulting in the bending Pacific plate, east of the interplate region of the large 1976/2021 thrust faulting sequences in the vicinity of Raoul Island. The outer trench slope faulting has involved temporally and spatially proximate pairs of large shallow normal faulting and deeper compressional faulting events (e.g., Christensen & Ruff, 1983, 1988; Todd & Lay, 2013; Ye et al., 2012; Ye, Lay, & Kanamori, 2021). The relatively rare occurrence of major deep compressional faulting below the trench slope has been attributed to the build-up of compressional stress from the locking of the megathrust being superimposed on elastic slab bending stresses, with the 2 July 1974 (M_S 7.3) intraplate compressional event occurring two years ahead of the 1976 sequence on the megathrust (e.g., Christensen & Ruff, 1988; Ye, Lay, & Kanamori, 2021). A ∼45 km deep compressional event on 21 October 2011 (M_W 7.4) followed an M_W 7.6 normal-faulting event at ∼20 km deep on 6 July 2011, and the shallow megathrust experienced many smaller thrust faulting events in this sequence extending from 12 to 30 km deep (Todd & Lay, 2013). This triggered thrusting indicates a strong susceptibility to moderate earthquake triggering in the shallow region along the crust/slab contact where no major or great thrust events have been recorded and most aftershock activity for the 2021 sequence was concentrated (Figures 2 and S2 in Supporting Information S1). Extensive background thrust activity has occurred along the shallow crust/slab interface (Figure S3 in Supporting Information S1), so it is very seismogenic, but it does not appear to be accumulating large strains to release in great events. There were only minor effects of the large 2011 events and the triggered megathrust activity in the Raoul displacement history (Figure 3a), so the slip deficit at this site was primarily due to megathrust locking at greater depth.

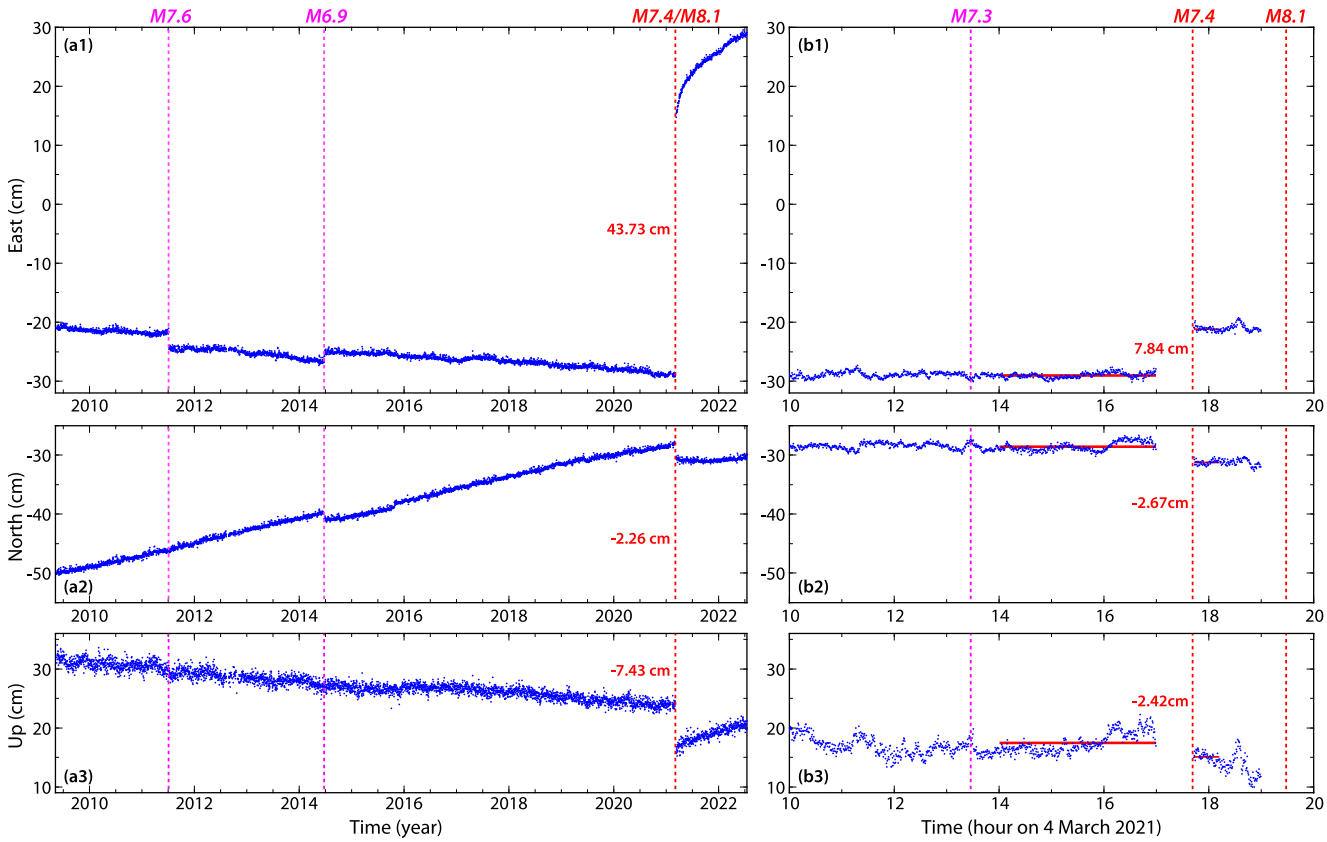

Figure 3. GNSS position at RAUL. (a1–a3) Long-term final daily solutions for the cleaned GNSS position at RAUL in the IGS14 from 2009, produced by the Nevada Geodetic Laboratory. The magenta vertical dashed lines indicate the 6 July 2011 M_W 7.6 and 24 June 2014 M_W 6.9 Kermadec earthquakes. The red vertical dashed line indicates the 2021 Kermadec sequence, with a time gap of one week from March 4th to March 11th. The general westward and northward motion of the station indicates accumulation of slip deficit on the megathrust boundary, with small offsets notable in 2011 and 2014, along with the large offsets on 4 March 2021, which captures the combined deformation of the foreshock and mainshock along with post-seismic deformation. The early 1-week postseismic deformation was not resolved due to instrumental failure. (b1–b3) 30-s solutions on 4 March 2021 processed by the Canadian Geodetic Survey of Natural Resources, Canada, Canadian Spatial Reference System Precise Point Positioning (CSRS-PPP) service. We correct the average baseline from 0:00 to 6:00 with the daily solutions from panels (a1, a2, and a3), respectively. The red bars show the average levels before and after the M_W 7.4 foreshock, and the estimated static offsets are 7.84 cm, −2.67 cm, and −2.42 cm in east, north, and upward directions, respectively. Using the total offsets from March 4th to March 11th in panels (a1–a3), we estimate that the static offsets are 35.89 cm, 0.41 cm, and −5.01 cm for the M_W 8.1 mainshock (Figure 4).

We analyze the rupture process of the 2021 northern Kermadec sequence using well-established seismic, geodetic, and tsunami modeling procedures, establishing that the large coseismic slip occurred along the mantle/slab contact. We then compare seismic recordings for the 2021 M_W 7.4/8.1 events with those for prior major megathrust earthquakes in the northern Kermadec region, particularly for events in the 1976 sequence, establishing that those events similarly occurred along the mantle/slab contact but were not "repeaters" in the sense of re-rupturing the same localized fault patches. We then consider the unusual frictional behavior indicated by such deep interplate ruptures in this region and the implications for other island arcs.

3. Data and Methods: Megathrust Rupture Quantification in Kermadec

3.1. Rupture Process of the 2021 M_W 7.4 Foreshock and M_W 8.1 Mainshock

Both the M_W 7.4 foreshock and M_W 8.1 mainshock involved low-angle thrust faulting (Table 1), indicating rupture on the subduction megathrust in northern Kermadec. For the foreshock, the *W*-phase inversion reported by the USGS-NEIC has a purely double couple solution with strike $\phi = 196°$, dip $\delta = 33°$ and rake $\lambda = 82°$, and seismic moment $M_0 = 1.465 \times 10^{20}$ N-m (M_{WW} 7.38), with a centroid depth of 45.5 km. The GCMT solution has a similar solution with $\phi = 201°$, $\delta = 29°$, $\lambda = 98°$, $M_0 = 1.79 \times 10^{20}$ N-m (M_W 7.4), centroid depth 42.8 km, and 15.5 s centroid time shift. For the mainshock, the *W*-phase inversion by the USGS-NEIC has an 89% double couple

Table 1
Point-Source Solutions for the Foreshock and Mainshock

	Lon.	Lat.	H (km)	Strike	Dip	Rake	M_0 (Nm)	M_W
Foreshock								
USGS	−177.10°	−29.67°	45.5	196.0°	33.0°	82.0°	1.47×10^{20}	7.38
GCMT	−177.01°	−29.58°	42.8	201.0°	29.0°	98.0°	1.79×10^{20}	7.40
Mainshock								
USGS	−177.10°	−29.53°	23.5	201.0°	16.0°	98.0°	2.03×10^{21}	8.14
GCMT	−176.73°	−29.11°	33.9	199.0°	19.0°	97.0°	1.60×10^{21}	8.10
This study			40.5	191.7°	22.6°	85.6°	1.39×10^{21}	8.03

solution with strike $\phi = 201°$, dip $\delta = 16°$, and rake $\lambda = 98°$, and seismic moment $M_0 = 2.033 \times 10^{21}$ N-m (M_{WW} 8.14). The centroid depth is 23.5 km. The GCMT solution has a similar solution with $\phi = 199°$, $\delta = 19°$, $\lambda = 97°$, $M_0 = 1.6 \times 10^{21}$ N-m (M_W 8.1), centroid depth 33.9 km, and 28.9 s centroid time shift. We perform a *W*-phase inversion (Kanamori & Rivera, 2008) for the mainshock using ground motions from 80 channels at 37 stations filtered in the bandpass 0.002–0.005 Hz, which gives a centroid depth of 40.5 km, with $\phi = 191.7°$, $\delta = 22.6°$, $\lambda = 85.6°$, $M_0 = 1.39 \times 10^{21}$ N-m (M_W 8.03). A very similar *W*-phase inversion with a centroid depth of 40.5 km is obtained using a much larger data set of 176 ground motion channels from 77 stations. Thus, we conclude that the centroid depth for the mainshock does appear to be deeper than the USGS-NEIC solution but shallower than the foreshock.

The USGS-NEIC computed initial planar finite-fault solutions for both the foreshock and mainshock using teleseismic body and surface waves, and we refine the source models for these two events by conducting joint inversion of teleseismic body waves and static ground motion recorded at a GNSS station RAUL located on Raoul Island, just to the west of both ruptures (Figure 3). We use the SLAB2 plate interface model (Hayes et al., 2018) to set up a 2.5D fault model surface which varies in dip with depth along the fault, along with variable bathymetry above the fault (Figure S4 in Supporting Information S1). Global broadband stations in the epicentral distance range of 30°–95° provide the seismic waveform data, with ground displacement motions filtered in the 0.005–0.9 Hz passband, used for finite-fault inversions. For the M_W 7.4 foreshock, we use 92 *P* waves and 40 *SH* waves with a good azimuthal distribution. For the mainshock, we use 92 *P* waves and 51 *SH* waves. Detailed waveform modeling results are given in Figures S5–S7 in Supporting Information S1 for several models.

Raoul Island, which lies to the northwest of the epicenters of the large events, is the site of a broadband seismic station (RAO) (Figure 2b) and GNSS station RAUL (Figure 4). The site was strongly impacted by shaking from the foreshock, and both sensors lost power after the mainshock. RAO did detect foreshock activity prior to the mainshock, although the BH1 and BHZ instrument masses were off-centered, and signals went off-scale for the mainshock, as discussed below. The 30-s solutions for ground motion for the foreshock were recovered from RAUL, but the coseismic motion of the mainshock was not recorded. By March 10, the power was restored, and the offset at RAUL from the combined events and the first 7 days of any afterslip could be measured, along with subsequent deformation from later afterslip (Figure 3). The coseismic slip of the mainshock is estimated by correcting the daily solution upon restoration of power for the coseismic motion of the foreshock, recognizing that there is likely some unresolved contribution from early afterslip in the mainshock measurement. Inversions are thus performed using only the teleseismic data as well as including the single GNSS station data.

Finite-fault space-time slip distributions are determined for the M_W 7.4 and M_W 8.1 events using a least-squares kinematic inversion parameterized with multiple rake-varying subfault source time function windows (e.g., Hartzell & Heaton, 1983; Kikuchi & Kanamori, 1991; Ye, Lay, et al., 2016) for the dip-varying 2.5-D model. We adapt the local 1D source velocity structures from Model Crust 1.0 (Laske et al., 2013) with variable bathymetry over the fault. Precise details of the source region velocity structure are not available, but this has a negligible effect on the teleseismic inversions.

For the M_W 7.4 foreshock, the rupture model has 15 subfaults along strike and 9 along dip with dimensions of 10×10 km^2 for each grid. The source time functions of the subfaults are represented by 16 symmetric triangles with 1.0-s rise times and 1.0-s time shifts, allowing maximum possible subfault durations of 17.0 s. Given the large

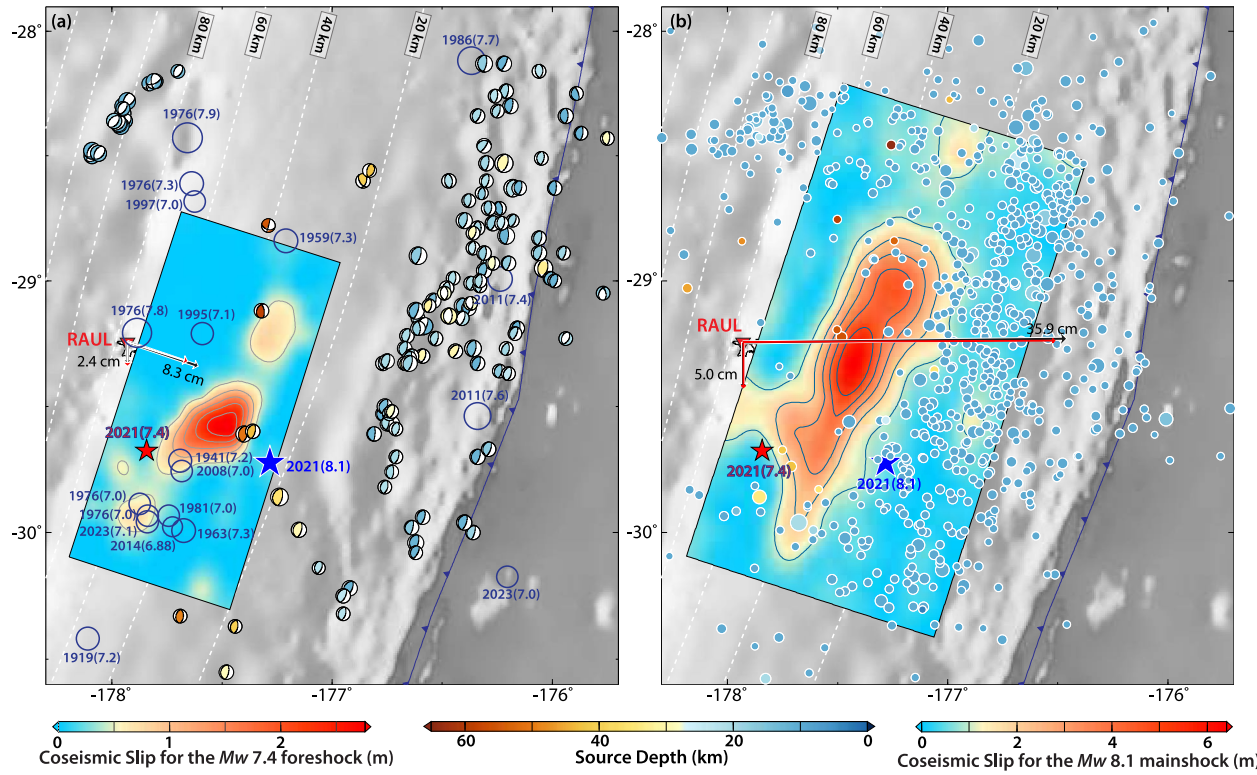

Figure 4. Map views of our preferred finite-fault slip models for (a) the M_W 7.4 foreshock and (b) the M_W 8.1 mainshock from the joint inversions with the fit to the GNSS station RAUL, along with USGS-NEIC aftershocks in the first 3 months. Red and blue stars indicate the epicenters of the M_W 7.4 and M_W 8.1 events, respectively. Historical USGS-NEIC activity with M7.0+ around the 2021 sequence is shown with dark blue circles, scaled proportional to magnitude. Available focal mechanisms from the GCMT catalog for 3-month aftershocks are shown in panel (a) at the GCMT centroid locations and aftershocks within the first 3 months from the USGS-NEIC catalog are shown in panel (b) at their epicenters. Both are color-coded with source depth. Dashed curves indicate the SLAB2 plate interface depth in 20-km increments. The inverted triangle locates GNSS station RAUL, with observed (black) and predicted (red) coseismic displacements. The horizontal and vertical displacements are shown by vectors pointing southeast/east and downward, respectively.

centroid depth, an upper bound of 4 km/s was imposed for the rupture speed, corresponding to the kinematically allowed rupture expansion. The joint inversion of seismic and geodetic data results in our preferred $M_0 = 1.9 \times 10^{20}$ Nm (M_W 7.45), a slip centroid depth of 39.0 km, and large-slip (>1 m) concentrated between 30 and 45 km depth (Figures 4a and S5 in Supporting Information S1). We find a peak slip of ~2.5 m in a concentrated slip patch located ~30 km northeast from the epicenter. For this slip model, the static stress drop estimates are 5.5 MPa for a slip-weighted distribution (energy-related stress drop) and 3.1 MPa for a circular model with area computed for the subfaults with more than 15% of the peak slip (following Ye, Lay, et al., 2016). The radiated energy estimated using the spectrum of the moment rate function for periods longer than 20 s and the average of propagation-corrected spectra of many broadband P waves for periods of 1–20 s is 1.63×10^{15} J, giving a moment-scaled value of 9.1×10^{-6}, typical of interplate thrust events (Ye, Lay, et al., 2016). Data fits are good for both seismic waveforms (Figure S5 in Supporting Information S1) and the coseismic displacements measured at the GNSS RAUL station (Figure 4a). The finite fault solution reported by the USGS-NEIC also features a dominant large-slip patch with up to 3 m slip located northeastward from the epicenter (https://earthquake.usgs.gov/earthquakes/eventpage/us7000dfk3/finite-fault). A finite-fault solution by Lythgoe et al. (2023) places a similar large-slip patch at larger depths from 50 to 60 km. The inclusion of the static deformation at the RAUL station is unique in this study, which provides a strong constraint on the downdip limit for the coseismic slip distribution.

For the M_W 8.1 mainshock, the grid network is comprised of 22 subfaults along strike and 13 along dip with dimensions of 10×10 km^2. The source time functions of the subfaults are represented by 14 2.5-s rise time symmetric triangles, with 2.5 s time shifts, giving maximum possible subfault durations of 37.5 s. We again assume a maximum rupture expanding speed of 4 km/s. The effective rupture speeds can be lower due to the multiple subfault subevents allowed, but there is very little resolution. Our preferred slip model from the joint inversion of seismic and geodetic data (Figures 4b and S6 in Supporting Information S1) has $M_0 = 1.62 \times 10^{21}$

Nm (M_W 8.07) and a slip centroid depth of 34.8 km. A peak slip of ~6 m is found in a concentrated large-slip patch extending down-dip and northeastward from the hypocenter. Slip exceeding 2 m extends from 20 to 55 km along dip. Negligible slip is located at shallow depths less than 20 km, similar to the foreshock. A similar slip model is obtained from teleseismic inversion by Zeng et al. (2025). The static stress drop estimates for this model are 6.6 MPa for the energy-related stress drop and 5.2 MPa for the equivalent circular model. The radiated energy estimated is 9.5×10^{15} J, giving a moment-scaled value of 5.9×10^{-6}, somewhat low relative to other interplate thrust events (Ye, Lay, et al., 2016). Inversion of just the seismic data gives a similar solution with a concentrated large-slip patch extending to the northeast of the hypocenter (Figure S7 in Supporting Information S1), and some weak shallow slip. The comparison between observed and predicted seismic waveforms for the joint inversion model is excellent (Figure S6 in Supporting Information S1) as are the waveform fits for the seismic data inversion only (Figure S7 in Supporting Information S1). While there is some uncertainty in the magnitude of the coseismic offset measured at the GNSS RAUL station due to the power outage interval, the direction of displacement (Figure 3a) provides a helpful constraint on the placement of slip on the fault for this event, and we prefer the joint inversion result. The USGS-NEIC finite fault solution has a slip patch with up to 4 m of slip downdip from the hypocenter extending northward in a similar location to our model, but also includes an up-dip slip patch south of 29°S, with up to 3 m that is not present in our inversions (https://earthquake.usgs.gov/earthquakes/eventpage/us7000dflf/finite-fault). A solution by Lythgoe et al. (2023) places a similarly shaped large-slip patch between 24 and 50 km depth, with minor patchy slip at <10 km depth. The primary mainshock slip is resolved by these finite-fault models, and the large slip is consistently deeper than the upper plate Moho depth at 17 km.

3.2. Tsunami Observations and Modeling for the 2021 M_W 8.1 Kermadec Earthquake

The M_W 8.1 mainshock produced a modest tsunami well recorded by the recently deployed New Zealand DART network (Fry et al., 2020; GNS Science, 2020) and by several tide gauges in New Zealand, Australia, Tonga, Vanuatu, New Caledonia, and southern New Hebrides (Wang et al., 2022). Romano et al. (2021) inverted 12 tsunami waveforms (DART and tide gauges) for a slip model with $M_0 = 1.15 \times 10^{21}$ Nm (M_W 8.0) featuring a dominant large-slip patch with peak slip of 5 m northeast of the hypocenter; the main asperity was concentrated from 20 to 30 km deep, generally similar to our finite-fault model. The seafloor deformation was less than 1.1 m, resulting in relatively weak tsunami excitation, ranging up to ~60 cm at the Kingston Jetty tide gauge on Norfolk Island to the west. As an independent verification of the seismo-geodetic slip model, we compare the closest tsunami observations (Figure 5) with the tsunami predicted using our preferred slip model (Figure 4b). The slip model is used to compute the coseismic seafloor deformation through the Okada (1985) analytical formulas, low-pass filtered to approximate non-hydrostatic tsunami generation (Kajiura, 1963), and used as the static initial condition for the simulation of tsunami propagation. The numerical simulation is performed with the multi-GPU Tsunami-HySEA code (de la Asuncion et al., 2013; Macias et al., 2017), solving the nonlinear shallow water equations. Here, we adopt a system with two levels of nested grids to better account for shoaling tsunami wavelength reduction; a coarse grid (1 arc-min spatial resolution, SRTM15, http://topex.ucsd.edu/www_html/srtm30_plus.html) for the tsunami modeling in the open ocean, and a finer one (15 arc-sec) for the areas around the tide gauges.

Overall, the tsunami simulation provides a reasonable agreement between observed and predicted tsunami waveforms in terms of amplitudes and shapes of the signals. The fit to DART observations is, as generally expected, better than for the tide gauges where the records are influenced by the interaction with the coastal morphology (Figure 5). A larger mismatch in time and amplitude can be due to a lack of resolution and inaccuracy of the bathymetry models adopted around the tide gauges or instrument clock issues (e.g., Romano et al., 2020), other unmodelled physical effects (Watada et al., 2014), and the trade-off between the propagation time and the absolute slip position. In particular, the time mismatches are in the range of several minutes for all of the stations, with the largest offsets observed at some tide gauges (Figure 5). Using *ad-hoc* cross-correlation time-shifts to align the waveform maxima, a common practice when bathymetric information is limited, we find that the data waveform fit is quite good (Figure 5). We note that the time shifts are, on average, several minutes greater than those found in the tsunami inversion by Romano et al. (2021) using the Optimal Tsunami Alignment approach (Romano et al., 2016, 2020). The slip model obtained by inverting only tsunami data does have the main slip patch displaced by ~10 km northwestward (Romano et al., 2021) with respect to the slip model obtained by jointly inverting the seismic and geodetic data in this study. The seismo-geodetic slip model only accounts for the minor

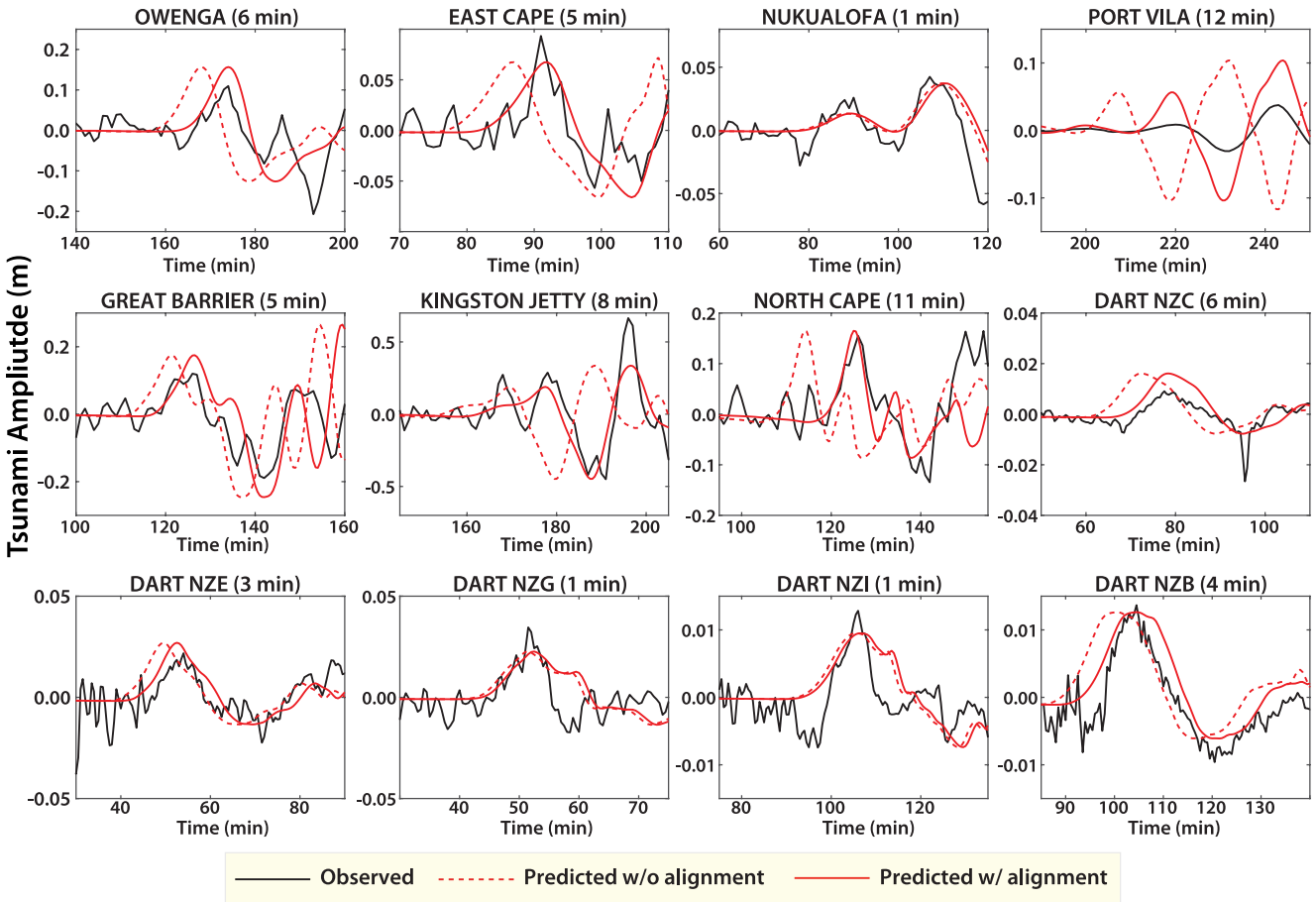

Figure 5. Waveform fitting of tsunami data by our preferred slip model for the M_W 8.1 mainshock. Black and red lines, respectively, show observed and predicted tsunami recordings at the tide-gauge and DART stations. The station locations are shown in Figure 1 in Romano et al. (2021). The model predictions are shown without (dashed red lines) and with (solid red lines) time shifts in minutes (indicated at the top of each panel) obtained by cross-correlation alignment. The comparisons validate our preferred slip model (Figure 4b).

discrepancies in modeling tsunami data. The tsunami predictions give a first-order validation of the seismic moment and the overall spatial extent of the source, including the lack of significant shallow slip, estimated by the seismo-geodetic inversion, although there is limited resolution of lower slip features in the model. Joint inversion of tsunami, seismic, and geodetic data in the future can be undertaken to fully reconcile all of the observations.

3.3. Other Inferences of Limited Shallow Slip During the M_W 8.1 Mainshock

The up-dip extent of megathrust slip is typically difficult to resolve in finite-fault inversions without having nearby tsunami observations (e.g., Bai et al., 2022). If some significant slip occurs at shallow depths close to the trench, strong water multiples (*pwP*) will be excited in the deep water. This generates ringing in the teleseismic *P* wave coda that exceeds the level excited if the slip is confined to greater depth (e.g., Lay et al., 2019). We examined azimuthally distributed *P* wave coda amplitudes relative to direct *P* amplitudes for the M_W 8.1 mainshock at epicentral distances from 80° to 120°, finding median ratios (~0.7) only slightly elevated relative to events for which no slip occurred on the shallow megathrust (Lay et al., 2019), but the larger values are dominated by stations at eastward azimuths toward which the water multiples are expected to sense the deep Kermadec trench. The median $m_B = 7.58$ for a period of 3.55 s (52 channels from 30° to 80°), and the coda magnitude *m_coda* median value of 7.08, gives *m_coda*-$m_B = -0.49$, which is more negative than the values for events with shallow slip (Lay et al., 2019). These observations are consistent with the primary large slip in the mainshock being located deeper on the megathrust as in our slip model (Figure 4b), and as also found in the tsunami inversion by Romano et al. (2021), although the latter model does have minor, weakly tsunamigenic slip of up to 0.5–1 m extending to the trench. Ruptures with large slip on the shallow megathrust often induce concentrations of outer

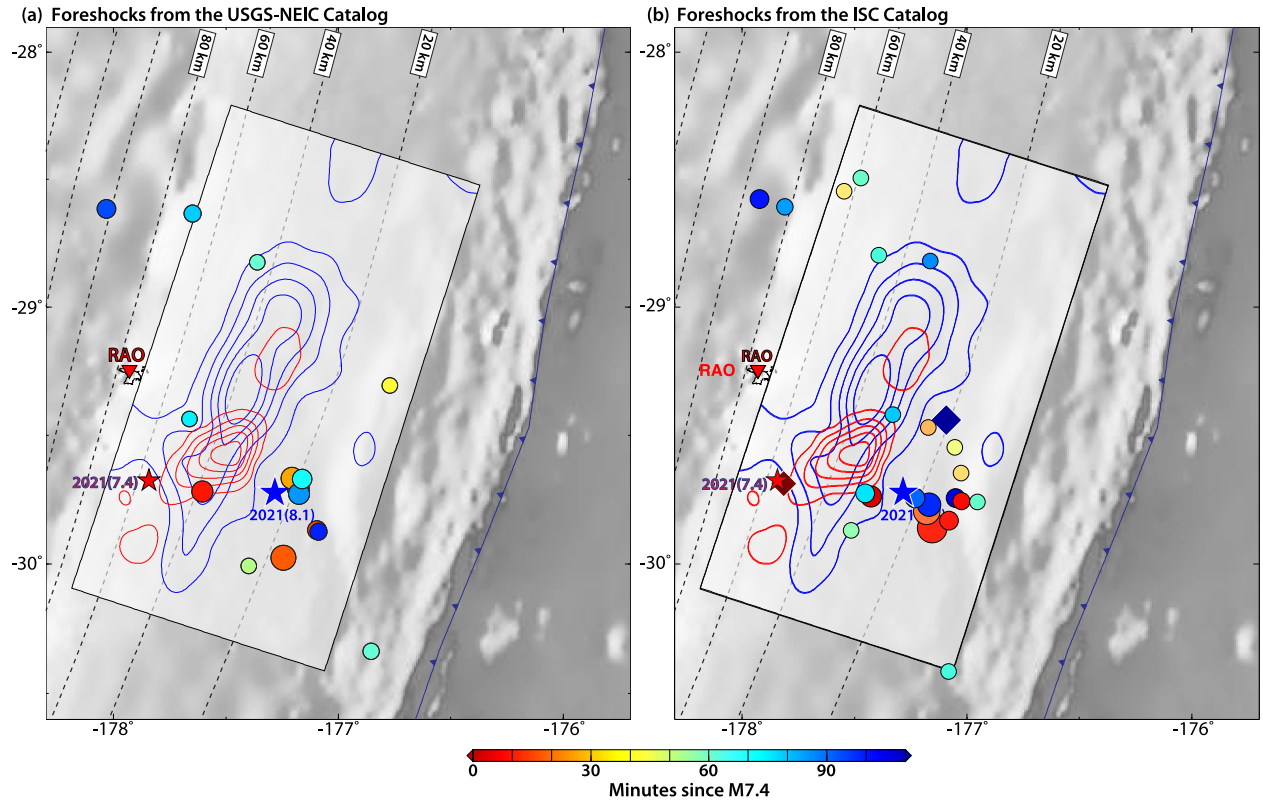

Figure 6. Locations of earthquakes following the M_W 7.4 foreshock and preceding the M_W 8.1 mainshock. (a) Events from the USGS-NEIC catalog are shown as circles, with small events color-coded by time after the M_W 7.4 foreshock. The USGS-NEIC foreshock epicenter is the red star, and the slip distribution of our preferred foreshock model is in red contours with 0.5-m interval. The USGS-NEIC mainshock epicenter is the blue star, and the slip distribution of our preferred mainshock model is in blue contours with 1-m interval. (b) Events from the ISC are shown as circles, with small events color-coded by time after the M_W 7.4 foreshock. Red and blue stars show the USGS-NEIC epicenters for the M_W 7.4 foreshock and the M_W 8.1 mainshock, and diamonds show the epicenters from the ISC catalog.

rise extensional faulting aftershocks up-dip of the shallow slip region (e.g., Sladen & Trevisan, 2018; Wetzler et al., 2017; Ye, Lay, & Kanamori, 2021). Only a handful of normal faulting aftershocks, all with $M_W \leq 5.5$, occurred seaward of the large-slip zone in the first 3 months (Figure 6a). This adds to the inference that coseismic large slip did not occur on the shallow megathrust along the crust/slab interface.

3.4. Aftershocks and Seismicity Between the Two Large Events

There is a clear paucity of prior seismicity in the vicinity of large-slip areas in the down-dip portion of the megathrust for both M_W 7.4/8.1 events (Figure 4). Almost all aftershocks along the megathrust are located shallower than ~30 km depth, up-dip of the slip zones of the two ruptures. There is a cluster of shallow crustal activity located further to the northwest. The large-slip zone of the foreshock overlaps a region that has moderate slip in the mainshock, and a secondary area of low slip in the foreshock overlaps the large slip zone in the mainshock (Figure 6). Despite the constraint offered by the inland GNSS stations, the resolution of absolute slip placement is limited (e.g., Romano et al., 2010). The vertical and horizontal displacements at RAUL do indicate that there is likely some overlap of slip between the two events, although the models of Lythgoe et al. (2023) without the constraint from the GNSS data have no overlap.

Comparison of the mainshock slip distribution with the spatial distribution of historical GCMT locations reinforces the complementarity of the smaller, shallow activity and the coseismic slip in the mainshock (Figure S3 in Supporting Information S1). A lack of aftershocks within the large-slip zone (Figure 4b) is a common observation for megathrust ruptures (e.g., Wetzler et al., 2018). Similar shallow aftershock distribution for a fairly deep rupture on the megathrust is also observed in the recent 2021 Chignik M_W 8.2 sequence (Ye et al., 2022), although fewer aftershocks occurred in the up-dip region for the 2020 M_W 7.8 comparably deep Shumagin rupture (Ye, Lay, Kanamori, Yamazaki, & Cheung, 2021).

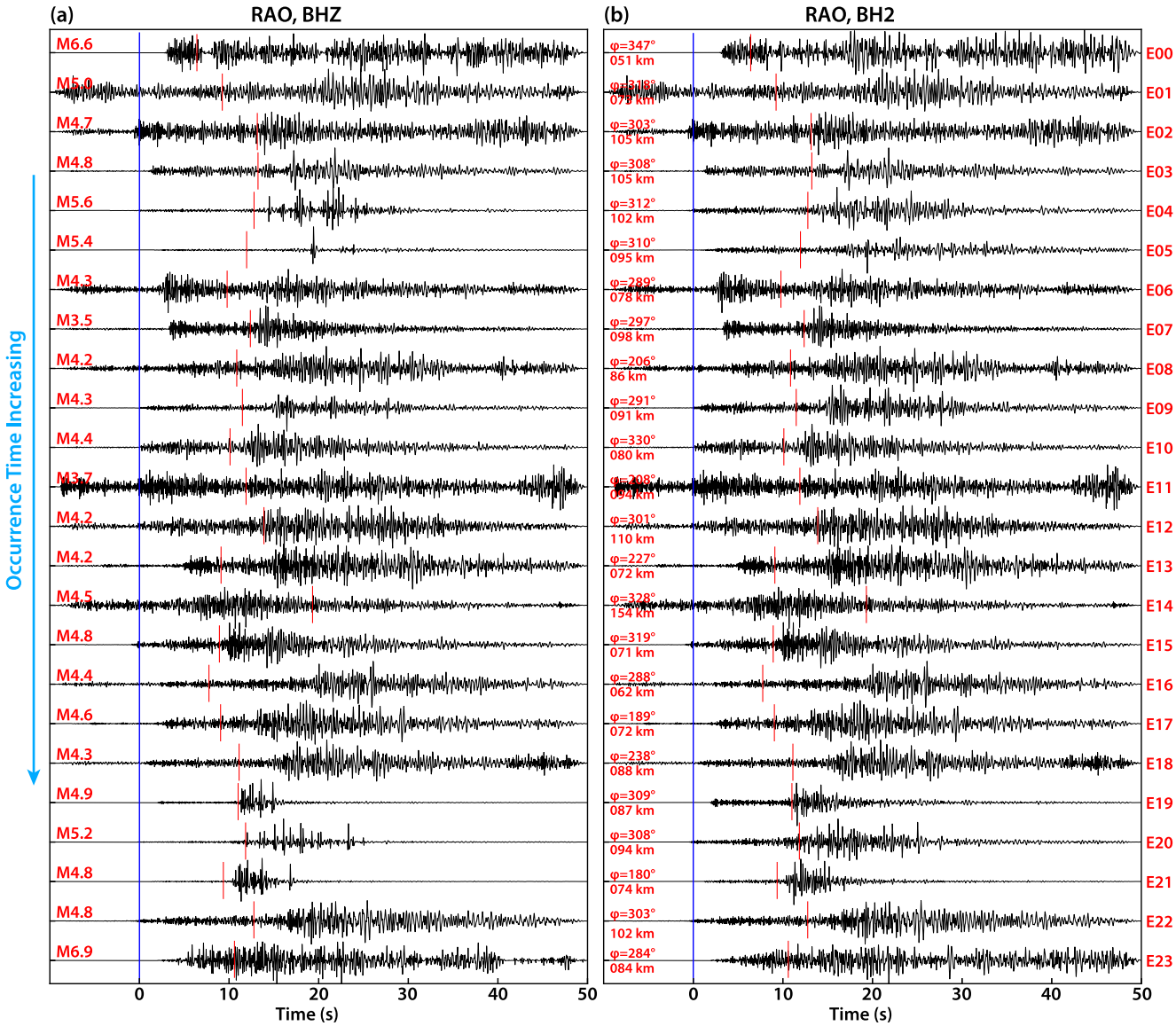

Figure 7. Seismic waveforms for events occurring between the M_W 7.4 foreshock (E00) and M_W 8.1 mainshock (E23) recorded by the broadband seismic station RAO on Raoul Island. The north component (BH1) failed in this <2 hr interval. Raw seismic data of vertical (BHZ) and east (BH2) components are filtered in the frequency band of 2.0–12.0 Hz. Earthquake magnitudes from the USGS-NEIC catalog are labeled in panel (a). Station azimuth and distance labeled in panel (b) are calculated with earthquake origin from the USGS-NEIC catalog.

For seismicity that occurred in the time between the foreshock and the mainshock, we consider both the USGS-NEIC and ISC (International Seismological Center) catalogs (Figure 6). There are 15 events in the USGS-NEIC catalog with magnitudes from 4.3 to 5.3, and 7 more events with magnitudes from 3.5 to 4.6 in the ISC catalog (Table S1 in Supporting Information S1). We confirm the existence of most reported events by inspecting the RAO waveforms (Figure 7). We then apply the EQTransformer algorithm for *P* and *S* arrival picking (Mousavi et al., 2020) and the REAL association algorithm (Zhang et al., 2025) to continuous waveform signals at RAO (the two working components) and at the next 23 closest three-component global stations (all more than 1,000 km away) (Figure S8 in Supporting Information S1). We identify 41 local events, 16 of which correspond to events from the ISC catalog (Figure S9 in Supporting Information S1). Attempts to relocate the 41 events with NonLinLoc (Lomax et al., 2000) prove very unstable due to the poor signal quality and emergent waveforms (Figure S10 in Supporting Information S1), which make it hard to ensure that the same arrival is picked teleseismically, so we do not succeed in refining the catalog location estimates. For both USGS-NEIC and ISC catalogs, most events lie eastward (up-dip) from the foreshock and mainshock hypocenters, and only a few events overlap the large-slip

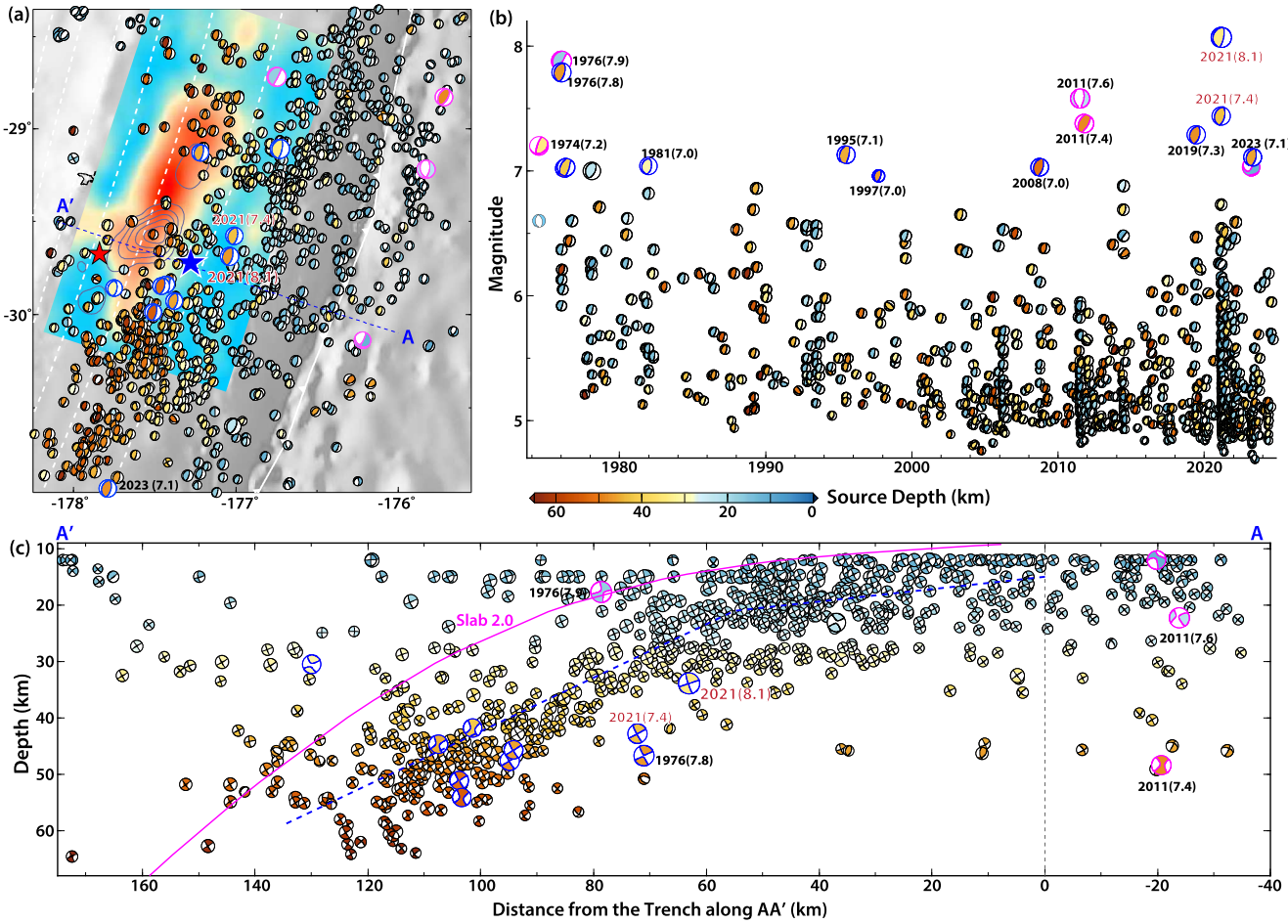

Figure 8. Focal mechanisms for earthquakes in the northern Kermadec subduction zone. (a) Map view of focal mechanisms for all earthquakes from the GCMT catalog since 1976 along with the slip distribution (contours and color palette) of our preferred model for the M_W 8.1 mainshock (Figure 4b) with hypocenter indicated by the blue star and the gray slip contours for the M_W 7.4 foreshock (Figure 4a) with hypocenter indicated by the red star. Large events with $M_W \geq 7.0$ are highlighted by blue/purple perimeters. (b) The time sequence of earthquake focal mechanisms for all earthquakes in panel (a) with the focal mechanism for 1974 M_W 7.2 and M_S 6.6 events from Chapple and Forsyth (1974). (c) Vertical cross-section for all focal mechanisms in panel (a) projected along AA′. The purple and dashed blue curves show the slab geometry adapted from the Slab 2.0 model (Hayes et al., 2018) and Lythgoe et al. (2023), respectively.

zone of the mainshock (Figure 6). About five of the events are in close proximity to the mainshock hypocenter, suggesting that the mainshock nucleation might have been influenced not only by the slip of the M_W 7.4 foreshock, but also by the cluster of shallow foreshock activity occurring within ~100 min beforehand. Given the limited information and uncertain locations of the foreshocks occurring between the M_W 7.4 foreshock and M_W 8.1 mainshock, the salient feature is the concentration of activity near the edge of the mainshock asperity, favoring a cascading sequence with stress triggering (e.g., Mignan, 2014).

3.5. Frequent Large Deep Megathrust Ruptures With Variable Dynamics

The depth-varying rupture characterization for megathrust ruptures (Lay et al., 2012) would identify the 2021 sequence as a Domain C rupture of the deep megathrust zone. The depth-varying focal mechanism distribution from the GCMT catalog suggests continuous thrusting activity along the megathrust, with larger events in a downdip region at depths from 30 to 50 km (Figure 8). While there may be minor along-strike variations in the slab interface position that contribute to the spread of locations, there is at least a ±5 km scatter in the depths for thrust events relative to any interface, and some events have even larger deviations of up to 30 km. Given the lack of nearby seismic stations, it is plausible that most of these involve mislocations from a single surface, but the possibility remains that there could be some intraplate activity with focal mechanisms similar to those of interplate thrusts. This has been found, for example, for the 3 May 2006 M_W 8.0 Tonga earthquake (Meng et al., 2015). The

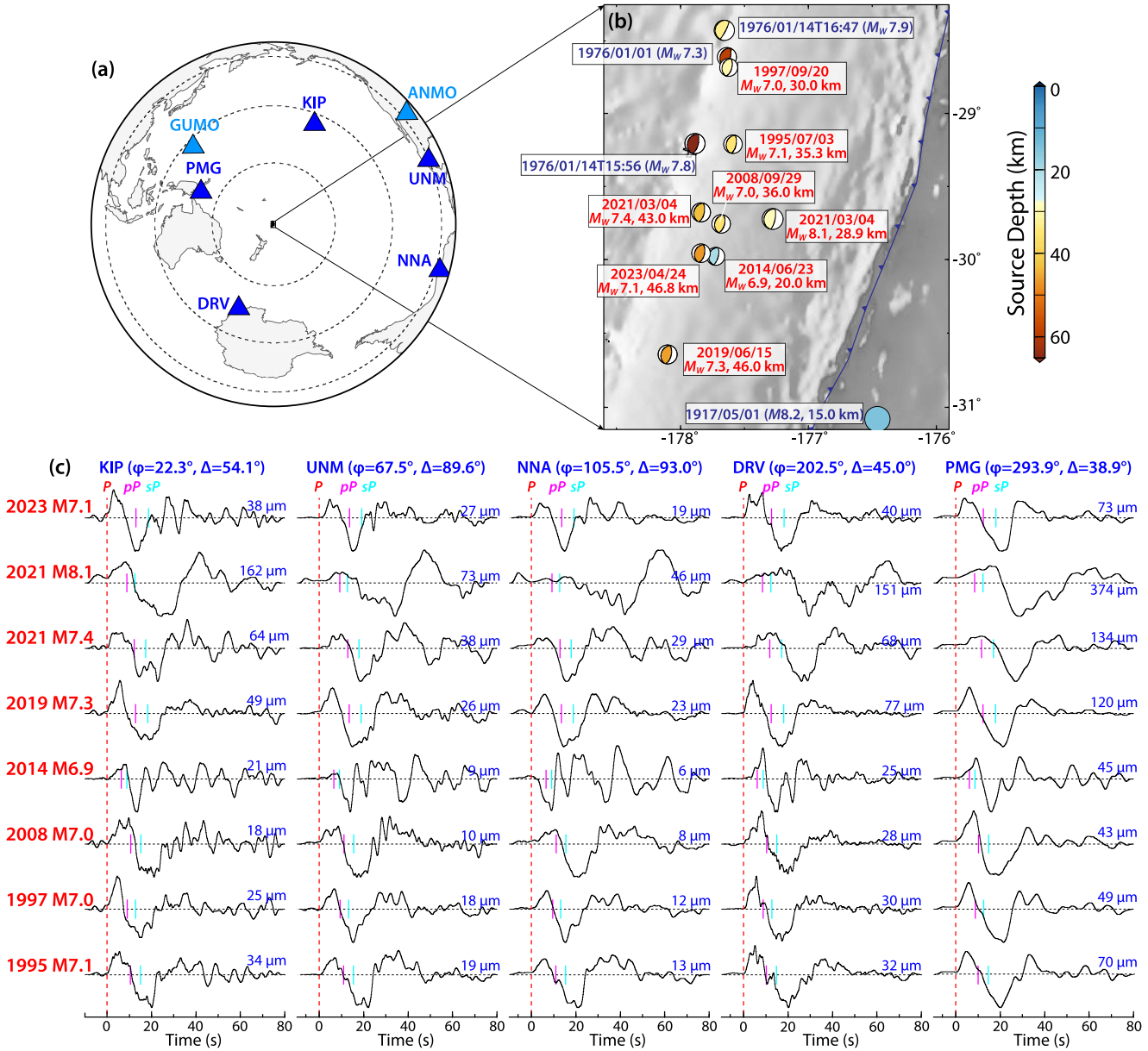

Figure 9. Sampled broadband teleseismic *P* waveforms for 8 major megathrust earthquakes in the Northern Kermadec since 1990. (a, b) Map view of earthquakes, 5 broadband seismic stations used in panel (c), and 2 seismic stations used for Figure 10. (c) Teleseismic *P* wave ground displacements filtered in the frequency band of 0.005–2.0 Hz. Waveforms are aligned with handpicked *P* arrivals with predicted *pP* (purple bars) and *sP* (cyan bars) time difference with source depths from the USGS-NEIC catalog and the IASP91 model. Waveforms are self-normalized with amplitude given at the end of each trace. Variations in waveforms might result from the difference in source depths and rupture complexity, thus they are not repeating or quasi-repeating ruptures.

outer trench normal and compressional faulting (Figure 8c) indicates that intraslab faults may be available for deeper reactivation of faulting, although not clearly with geometry similar to the plate boundary. Lythgoe et al. (2023) relocated larger aftershocks for the 2021 sequence using cut-and-paste inversions, *P* wave modeling, and surface wave master event locations, finding improved localization onto a dipping surface that supports the idea that mislocation blurs the slab interface (Figure 8). The same is true for large events in the 1976 sequence. Within relocation uncertainty, Lythgoe et al. (2023) infer substantial overlap of the 1976 and 2021 large ruptures. They conclude that the time history of $M_W \geq 5.5$ activity in the northern Kermadec region (Figure 8b) appears to comprise a 45-year-long seismic cycle in northern Kermadec. We also note that major interplate ruptures in northern Kermadec are spread through the 300 km long region from 28°S to 31°S with 8 events with $M_W \geq 6.9$ from 1990 to 2023 including the 2021 M_W 7.4/8.1 events, in addition to the 1976 thrusting sequence (Figure 9b). Given

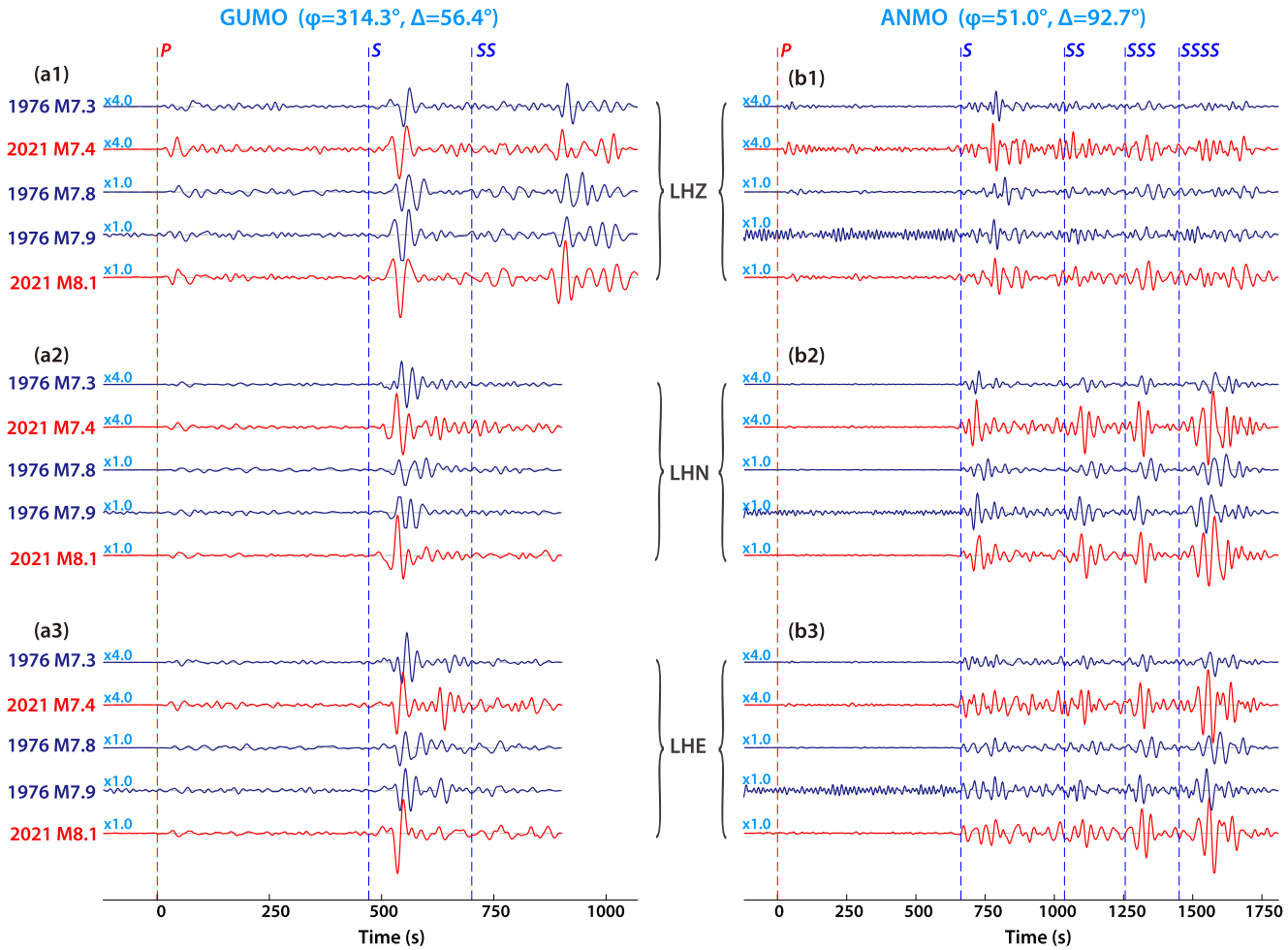

Figure 10. Comparisons of seismic waveforms with the SRO instrumental response between the 1976 and 2021 major earthquakes. (a1–a3) and (b1–b3) Three-component records at stations GUMO and ANMO, respectively. Waveforms for the 2021 events are simulated from the GSN broadband records by deconvolution of the instrumental response and convolution of the SRO instrumental responses for the 1976 events. Five traces in each panel share a common scale, with the amplitude for the 1976 M_W 7.3 and 2021 M_W 7.4 multiplied by 4. Waveforms are cut before the clipped segment for the 1976 events (see the raw data in Figure S12 in Supporting Information S1). Similar arrivals and relative amplitudes for different phases between the 5 major earthquakes are consistent with proximate location and magnitude difference, but not as repeating or quasi-repeating ruptures.

the location uncertainties, in order to assess whether there have been repeated ruptures in some areas, we consider a direct comparison of broadband seismic waveforms for those 8 events since 1990 (Figure 9). While the waveforms are all consistent with underthrusting, the waveforms vary in detail, supporting the notion that there are discrete patches of slip distributed throughout the region. We do not observe unambiguous repeating waveforms with very high waveform correlations for these large events.

Given that it appears that the 1976 sequence spanned about the same region as the 2021 sequence, it is also of value to compare waveforms from that sequence to those for the 2021 sequence. Fortunately, a good number of digital recordings are available for the major events in 1976 (Figure S11 and Table S2 in Supporting Information S1). Surface waves from the larger 1976 M_W 7.8 and 7.9 events clip at most stations (Figure S12 in Supporting Information S1), and some stations lack co-located broadband recording for the 2021 events, so a nearby station had to be used for comparison. The 2021 recordings were adjusted to have the same instrumental responses as the 1976 recordings following the procedure in Ye, Lay, et al. (2016), Ye, Kanamori, et al. (2016). We show comparisons of unclipped three-component body wave intervals for the three largest 1976 events with the two largest 2021 events at stations GUMO and ANMO (Figure 10). The *P* and *S* waveforms at both stations show significant differences, with the two, partially overlapping, 2021 events having the most similarity despite their size difference. Additional comparisons are shown for stations fairly closeby for the 2021 sequence in Figure S13

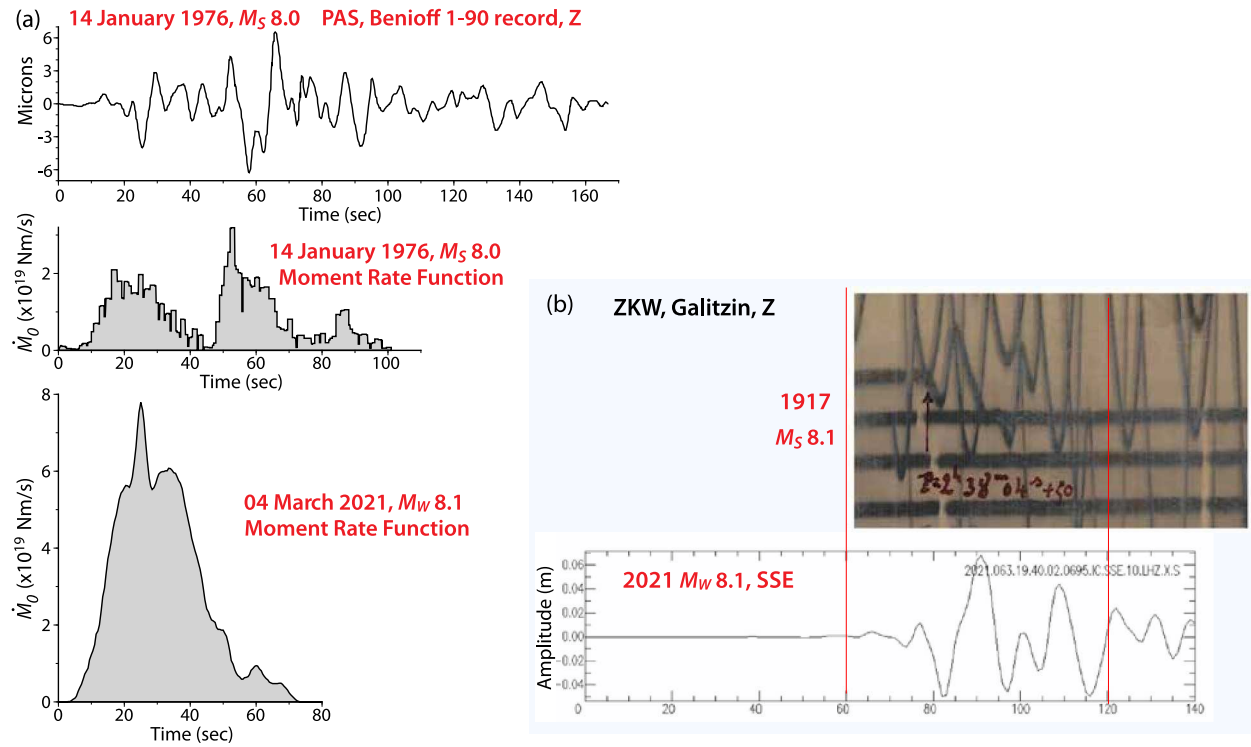

Figure 11. Seismic comparisons between the 2021 M_W 8.1 earthquake and historical great earthquakes in 1917 and 1976 in the northern Kermadec subduction zone. (a) Comparison of the moment rate function for the 14 January 1976 M_S 8.0 (likely M_W 7.8 at 15:56:33 UTC) (middle row) obtained by deconvolution of the single long-period Benioff (1–90) vertical component recording at station PAS (top row) by Hartzell and Heaton (1985), and the moment rate function for the 4 March 2021 M_W 8.1 mainshock from the joint inversion in this study (Figure 4b). The peak amplitude of the 1976 PAS seismogram is in microns for unit gain. (b) Vertical component Gallitzin recording at station ZKW in Shanghai, China, for the 1917 M_S 8.1 earthquake with the first *P* arrival indicating downward motion. Prediction of the Gallitzin recording for the 2021 M_W 8.1 mainshock with the ground motion at nearby SSE station in Shanghai (bottom row) has initial upward *P* motion at ~73 s, suggesting different focal mechanisms between the 1917 and 2021 events.

in Supporting Information S1. Lythgoe et al. (2023) show additional comparisons at station MAT. Recordings at the High Gain Long Period network stations experienced extensive clipping (Figure S14 in Supporting Information S1) and only a few components can be compared for the M_W 7.9 event due to contamination by the coda from the 51 min earlier M_W 7.8 event (Figure S15 in Supporting Information S1). Waveforms from two additional stations operating in 1976 that lack instrument information are shown in Figure S16 in Supporting Information S1. The differences in waveforms between the 1976 and 2021 sequences argue against simple re-rupture of persistent isolated asperities in the two sequences.

Finite-fault solutions for the 1976 doublet events have not been produced due to the limited data availability. The GCMT centroid for the 14 January 1976 M_W 7.8 event is near Raoul Island with a large depth, and this event has the closest relocation relative to the 2021 mainshock (Lythgoe et al., 2023), so it is possible that rupture did partly overlap the 2021 sequence. A single-station moment rate function deconvolution of the long-period (1–90 s) Benioff record (Hartzell & Heaton, 1985) assumed to be for the 14 January 1976 (15:56:34 UTC) M_W 7.8 event shows two main subevents (Figure 11a) with a total duration of ~75 s and a peak moment rate of ~3.2×10^{19} N-m/s (Hartzell & Heaton, 1985). In contrast, the moment rate function from the finite-fault inversion for the 2021 M_W 8.1 mainshock has a single large pulse with a duration of ~70 s and a peak moment rate of 7.8×10^{19} N-m/s. The total moments for the two earthquakes are similar, but assuming that the PAS deconvolution is reliable, the ruptures are very different.

3.6. The 1917 M_S 8.1 Event

The other large historical northern Kermadec earthquake of interest is the 1 May 1917 event with M_S 8.1, M_W 8.2 (ISC-GEM). The epicenter of this event from ISC-GEM, as reported by the USGS-NEIC, is (31.080°S, 176.461°W), placing it east of the trench south of the 2021 rupture zone (Figure 2b). A review of Gutenberg's

Notepads 32 and 77, currently archived at the Seismological Laboratory at California Institution of Technology, shows that he initially estimated an epicenter of (29.2°S 177°W) (Notepad 32), which was relocated to (31°S, 179°W), but the location using some additional data in Notepad 77 gives (29°S, 177°W), close to the initial estimate. Okal et al. (2011) relocated the event at (29.39°S, 179.29°W), about 100 km west of Raoul Island, but the large uncertainty ellipse overlaps the subduction zone. Overall, there is substantial uncertainty in the location of this event.

We collected and examined several recordings of the 1917 event, comparing the historical records with predictions from the 2021 mainshock using the broadband seismic record at the nearby SSE station equalized to the same instrument responses (following the procedure in Ye, Kanamori, et al., 2016) (Figure 11b). The vertical component Galitzin recording at station ZKW in Shanghai, China (31.19°N, 120.43°E) indicates a sharp (impulsive) downward motion for the first arrival, whereas a positive arrival would be expected for a shallow-dipping thrust mechanism, as shown for the 2021 M_W 8.1 mainshock with an emergent upward beginning of the SSE record at around 60–75 s. This raises the possibility that the 1917 event had a different focal mechanism. Okal et al. (2011) show a PKP arrival at De Bilt (DBN), which is compressional, which they interpreted as favoring a thrust mechanism. We note that the large M_W 7.7 event in 1986 to the northeast involved oblique compressional intraslab rupture (Figure 2b), which could account for such variable first-motion observations. The overall information has substantial uncertainty, and it remains ambiguous whether the 1917 event ruptured the same region as the 1976 and 2021 sequences, or is even an interplate rupture.

4. Discussion and Implication: Rupture on the Mantle/Slab Contact

The Moho depth of the overlying plate around the M_W 8.1 mainshock in the 2021 northern Kermadec sequence near 28°S is determined by several studies, with estimates of ∼17 km from a seismic reflection profile near 29°S (Bassett et al., 2016), ∼15–17 km from OBS data and gravity data (Funnell et al., 2017), and ∼17 km from multiple channel seismic data (Funnell et al., 2013). The 2011 M_W 7.4 foreshock and M_W 8.1 mainshock thus appear to have ruptured with the large slip located at greater depth than the overriding plate Moho, and this appears to have been the case for the major events in the 1976 sequence as well as for other major thrusts between 28°S and 31°S (Figure 8). Aftershocks for the 2021 sequence are located at shallower depths on the megathrust along the crust/slab boundary. Along with shallow megathrust aftershocks following large intraplate events in 2011 (Todd & Lay, 2013), this activity indicates a strong susceptibility to triggering with relatively weak and patchy coupling along the shallow crust/slab interface. Figure 12b schematically illustrates these attributes of the northern Kermadec plate interface, with it being the only documented subduction zone for which the largest interplate thrusts have been located along the mantle/slab interface.

Given the large age (>80 Ma) of the underthrusting oceanic plate, the temperature structure is relatively low in the northern Kermadec arc, but this should not preclude serpentinization of the shallow forearc mantle wedge and along the plate interface as long as aqueous fluids are released by the slab. It is plausible that no metamorphic fluids have been released from the slab locally, causing this region to be anomalous. However, the occurrence of large outer rise faulting, which can abet hydration of the slab and provide pathways for subsequent release of aqueous fluids at depth, and the presence of recent back-arc spreading with attendant circulation within the wedge, support the likelihood of hydration of the forearc mantle by slab fluids released due to porosity collapse with increasing pressure.

To illustrate rupture on the mantle/slab contact, P-T trajectories of the subduction interface are calculated based on the thermal model for northern Kermadec from Gao and Wang (2014) with preferred effective coefficients of friction (0.07) and another two values (0.04 and 0.10), relative to the serpentine phase diagram (Figure 12a). The phase transition diagrams of the serpentine minerals along the Kermedec megathrust are complex. We indicate some published conditions for the phase transition from low-temperature lizardite to high-temperature antigorite from Evans (2004) and from Schwartz et al. (2013) based on Alpine serpentinite, and the P-T conditions of the antigorite breakdown reactions are from Schmidt and Poli (1998) and Kitahara et al. (1966), following Wang et al. (2020). For the depth range of the large slip in the 2021 sequence, transition from lizardite to antigorite might have occurred, and antigorite is likely widespread along the mantle/slab contact, especially if the friction coefficient is 0.07 or higher (Figure 12a). Further studies with more appropriate slab geometry, fault zone rheology, rupture dynamics, and phase transition diagrams for serpentine minerals for the Kermadec subduction are warranted.

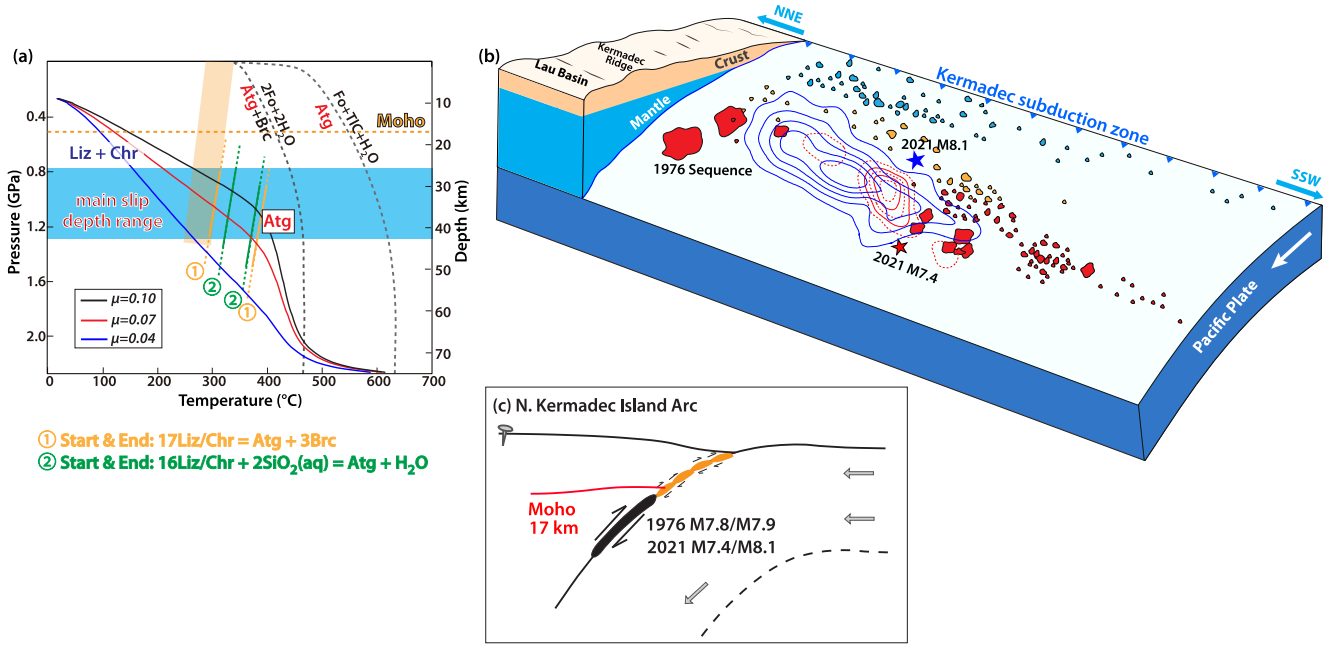

Figure 12. Rupture characteristics in the northern Kermadec subduction zone. (a) Simplified phase diagram of serpentine phases adapted from Wang et al. (2020). Atg = Antigorite, Brc = Brucite, Chr = Chrysotile, Fo = Forsterite, Liz = Lizardite, Tlc = Talc. The brown band shows the low-temperature Liz + Chr to high-temperature Atg phase transition as proposed by Evans (2004). Paired brown and green lines show the P-T domains of the start (left) and end (right) of the phase transitions from the Liz/Chr to Atg either without aqueous SiO_2(①) or with aqueous SiO_2 (②), adapted from the more recent work of Schwartz et al. (2013). The black dashed lines show antigorite breakdown reactions by Schmidt and Poli (1998) and Kitahara et al. (1966). Blue, red, and black curves show temperatures predicted by thermal models for the northern Kermadec megathrust with different effective coefficients of friction from Gao and Wang (2014). The dashed brown line indicates the Moho depth of ∼17 km from Bassett et al. (2016). The depth range for major earthquake ruptures for the northern Kermadec megathrust is shown by the blue band. (b, c) Schematic pattern of earthquake rupture along the northern Kermadec megathrust. The Moho depth of the overlying plate with contact with the slab is ∼17 km, as shown in panel (c). The slip model contours for the 2021 sequence foreshock (red curves) and mainshock (blue curves) from our preferred models (Figure 4) are shown. Red patches depict approximate main asperity areas of the 1976 sequence and other major earthquakes to the SSW of the 2021 sequence (Figure 8). Yellow and blue patches indicate the up-dip concentration of aftershocks for the 2021 sequence as shown in Figures 2 and 4, approximately along the mantle/slab (yellow: 17–25 km deep) and crust/slab (blue, <17 km deep) interfaces.

At low strain rates, lizardite has been shown to have plastic deformation with no evidence of brittle failure (e.g., Amiguet et al., 2012; Kaproth & Marone, 2013). Laboratory friction studies of antigorite initially showed that it is velocity-strengthening when loaded at tectonic slip rates (e.g., Moore et al., 1987; Reinen et al., 1994), and serpentinization has been invoked as a source of slow slip events (e.g., Goswami & Barbot, 2018; Liu et al., 2023; Okazaki & Katayama, 2014). However, at the high rate, the slip of antigorite-rich fault gouge is accompanied by dynamic strong drops in coefficients of friction to as low as 0.1 (Hirose & Bystricky, 2007; Kohli et al., 2011; Proctor et al., 2014), possibly due to flash heating (Brantut et al., 2016; Hirose & Bystricky, 2007). At temperatures 450°C and higher antigorite gouge has been found to change from flow behavior to stick-slip behavior (e.g., Takahashi et al., 2011). Proctor and Hirth (2016) find that antigorite-rich serpentinite gouge undergoes a transition from ductile to brittle deformation with temperature increasing from 300°C to 500°C. Albeit large uncertainty exists in laboratory results with variable in-situ conditions, we can infer that antigorite at certain temperatures may facilitate rupture along the mantle/slab contact. A fuller discussion of the serpentine mineral frictional behavior in this context can be found in Wang et al. (2025) which used the Chile margin for a case study of ocean-continent subduction, and we have considered whether similar concepts can work for ocean-ocean subduction zone (island arc) in the northern Kermadec region.

The investigation of the slip and seismicity distributions reported here cannot establish the mineralogy along the mantle/slab contact in the northern Kermadec region nor the extent of fluid release from the slab without the in-situ composition of the mantle/slab contact zone, but it is reasonable to speculate on the relationship between seismic observations and the thermally predicted serpentine mineralogy; the relatively low temperature (300–400°C) environment influences serpentinization and coupling on the boundary. It appears that the regions accumulating strain for large and great earthquakes on the mantle/slab interface are quite heterogeneous over a

300-km-long region based on waveform comparisons. Precisely why this results in distinct behavior from elsewhere along the Tonga-Kermadec zone and other island arc environments that also feature an old subducting slab is unclear, but possibly patchy high slip velocity failure of strong dynamic weakening antigorite-rich gouge can account for the local behavior.

5. Conclusions

The 2021 northern Kermadec interplate thrust sequence involved the largest known megathrust rupture along the Tonga-Kermadec subduction zone. Interseismic strain accumulation had been documented in the source region geodetically. Prior large earthquakes have struck the same general region in 1976 and 1917, but it does not appear that the earthquakes are strict repeaters based on seismic waveforms and locations for the earlier events. The large-slip regions of the 2021 M_W 7.4 foreshock and M_W 8.1 mainshock are located at depths of 20–55 km, along the mantle/slab interface below the 17 km deep upper plate Moho. The forward tsunami prediction by our seismo-geodetic slip model for the M_W 8.1 mainshock validates to the first order the seismic moment and the rupture extent of the finite-source model. The relatively large depths of slip on the megathrust reduced the tsunami excitation and regional tsunami hazard. The shallower megathrust has hosted extensive prior moderate seismic activity as well as most aftershock activity. As much as 2.7 m of slip deficit could have accumulated since the 1976 ruptures, but the peak slip in the 2021 events appears to be about twice as much, which further suggests that the ruptures do not involve simple recurrent failure of a persistent asperity. This is further supported by the discrepancy in their seismic waveforms. The 1917 event has a highly uncertain location and mechanism, but available waveform evidence favors it being an intraplate rupture north of the 2021 sequence. This leaves uncertainty in any assessment of the recurrence interval for the failure of any given portion of the megathrust. Eight M6.9+ deep megathrust earthquakes since 1990 in northern Kermadec are spread through the 300 km long region from 28°S to 31°S, in addition to the 1976 thrusting sequence, but display variable rupture dynamics. The occurrence of this frequent deep megathrust rupture in an oceanic subduction zone demonstrates that large earthquakes are not necessarily constrained to the shallow depth range of the crust/slab contact, and that extensive weakening of the deeper interface cannot be assumed when an old ocean plate is subducting. This enigmatic earthquake sequence raises concerns about the rupture potential for the deep portion of the megathrust with mantle/slab contact in island arcs, such as the Izu, Marianas, and Tonga zones, to accumulate large strain and produce infrequent great deep megathrust ruptures despite the lack of historical events in those regions. A specific explanation for the high rate of large events on the deep megathrust in northern Kermadec remains to be clarified.

Data Availability Statement

All body wave and surface wave recordings from global seismic stations that were used were downloaded from the Incorporated Research Institutions for Seismology (IRIS) data management center (IRIS, 2025). This included stations from Global Seismographic Network (II, IU), and International Federation of Digital Seismic Networks (FDSN) (AU, AZ, C1, CI, CM, CN, CU, DK, G, GE, IC and JP) as well as High Gain Long Period (HG) stations. We thank the facilities of IRIS Data Services, and specifically the IRIS Data Management Center, which were used for access to waveforms, related metadata, and/or derived products used in this study. IRIS Data Services are funded through the Seismological Facilities for the Advancement of Geoscience (SAGE) Award of the National Science Foundation under Cooperative Support Agreement EAR-1851048. Earthquake source mechanisms from the Global Centroid Moment Tensor project (Ekström et al., 2012) were used in this paper. Earthquake information is based on the catalogs of the National Earthquake Information Center at the U.S. Geological Survey (USGS-NEIC, 2025) and International Seismological Center (ISC, 2025). Kristine Larson provided the RAUL 30-s GPS signals, processed by the Canadian Geodetic Survey of Natural Resources, Canada, Canadian Spatial Reference System Precise Point Positioning service (CSRS-PPP, 2025). Daily solutions for RAUL were obtained from the Nevada Geodetic Laboratory (NGL, 2025). Tide gauge sea level data are obtained from IOC UNESCO (2025); New Zealand DART data are from GNS Science (2020). This work made use of GMT (Wessel et al., 2019) and SAC (Goldstein et al., 2003).

Acknowledgments
We thank Laura M. Wallace, Kelin Wang, Emily Brodsky, Heather Savage, Shiqing Xu, and Jeff Freymueller for helpful discussions, the editor Satoshi Ide, the associate editor, and anonymous reviewers for their thoughtful comments and suggestions which helped improve the manuscript. The work was supported in part by National Key R&D Program of China 2023YFF0803200 (L. Y.), National Natural Science Foundation of China (42474077, 42494864, 42494860, and 42106074), and National Science Foundation Grant EAR1802364 (T. L.).

References

Amiguet, E., Reynard, B., Caracas, R., Van de Moortele, B., Hilairet, N., & Wang, Y. (2012). Creep of phyllosilicates at the onset of plate tectonics. *Earth and Planetary Science Letters*, *345–348*, 142–150. https://doi.org/10.1016/j.epsl.2012.06.033

Bai, Y., Liu, C., Lay, T., Cheung, K. F., & Ye, L. (2022). Optimizing a model of coseismic rupture for the 22 July 2020 M_W 7.8 Simeonof earthquake by exploiting acute sensitivity of tsunami excitation across the shelf break. *Journal of Geophysical Research: Solid Earth*, *127*(7), e2022JB024484. https://doi.org/10.1029/2022jb024484

Bassett, D., Kopp, H., Sutherland, R., Henrys, S., Watts, A. B., Timm, C., et al. (2016). Crustal structure of the Kermadec arc from MANGO seismic refraction profiles. *Journal of Geophysical Research: Solid Earth*, *121*(10), 7514–7546. https://doi.org/10.1002/2016jb013194

Bevis, M., Taylor, F. W., Schutz, B. E., Recy, J., Isacks, B. L., Helu, S., et al. (1995). Geodetic observations of very rapid convergence and back-arc extension of the Tonga arc. *Nature*, *374*(6519), 249–251. https://doi.org/10.1038/374249a0

Blakely, R. J., Brocher, T. M., & Wells, R. E. (2005). Subduction-zone magnetic anomalies and implications for hydrated forearc mantle. *Geology*, *33*(6), 33445–33448. https://doi.org/10.1130/g21447.1

Bostock, M. G., Hyndman, R. D., Rondenay, S., & Peacock, S. M. (2002). An inverted continental Moho and serpentinization of the forearc mantle. *Nature*, *417*(6888), 536–538. https://doi.org/10.1038/417536a

Brantut, N., Passelegue, X., Deldicque, D., Rouzaud, J.-N., & Schubnel, A. (2016). Dynamic weakening and amorphization in serpentinite during laboratory earthquakes. *Geology*, *44*(8), 607–610. https://doi.org/10.1130/g37932.1

Canadian Spatial Reference System Precise Point Positioning service (CSRS-PPP). (2025). Global navigation satellite systems (GNSS) data post-processing [Dataset]. https://webapp.geod.nrcan.gc.ca/geod/tools-outils/ppp.php

Chlieh, M., Perfettini, H., Tavera, H., Avouac, J.-P., Remy, D., Nocquet, J.-M., et al. (2011). Interseismic coupling and seismic potential along the Central Andes subduction zone. *Journal of Geophysical Research: Solid Earth*, *116*(B12), B12405. https://doi.org/10.1029/2010jb008166

Christensen, D. H., & Lay, T. (1988). Large earthquakes in the Tonga region associated with the subduction of the Louisville Ridge. *Journal of Geophysical Research: Solid Earth*, *93*(B11), 13367–13389. https://doi.org/10.1029/jb093ib11p13367

Christensen, D. H., & Ruff, L. J. (1983). Outer-rise earthquakes and seismic coupling. *Geophysical Research Letters*, *10*(8), 697–700. https://doi.org/10.1029/gl010i008p00697

Christensen, D. H., & Ruff, L. J. (1988). Seismic coupling and outer rise earthquakes. *Journal of Geophysical Research: Solid Earth*, *93*(B11), 13421–13444. https://doi.org/10.1029/jb093ib11p13421

de la Asunción, M., Castro, M. J., Fernández-Nieto, E. D., Mantas, J. M., Acosta, S. O., & González-Vida, J. M. (2013). Efficient GPU implementation of a two waves TVD-WAF method for the two-dimensional one layer shallow water system on structured meshes. *Computers & Fluids*, *80*, 441–452. https://doi.org/10.1016/j.compfluid.2012.01.012

Delouis, B., Pardo, M., Legrand, D., & Monfret, T. (2009). The M_W 7.7 Tocopilla earthquake of 14 November 2007 at the southern edge of the northern Chile seismic gap: Rupture in the deep part of the coupled plate interface. *Bulletin of the Seismological Society of America*, *99*(1), 87–94. https://doi.org/10.1785/0120080192

DeMets, C., Gordon, R. G., & Argus, D. F. (2010). Geologically current plate motions. *Geophysical Journal International*, *181*(1), 1–80. https://doi.org/10.1111/j.1365-246x.2009.04491.x

Deschamps, F., Godard, M., Guillot, S., & Hattori, K. (2013). Geochemistry of subduction zone serpentinites: A review. *Lithos*, *178*, 96–127. https://doi.org/10.1016/j.lithos.2013.05.019

Eissler, H., & Kanamori, H. (1982). A large normal-fault earthquake at the junction of the Tonga trench and the Louisville ridge. *Physics of the Earth and Planetary Interiors*, *29*(2), 161–172. https://doi.org/10.1016/0031-9201(82)90070-x

Ekström, G., Nettles, M., & Dziewoński, A. M. (2012). The global CMT project 2004–2010: Centroid-moment tensors for 13,017 earthquakes. *Physics of the Earth and Planetary Interiors*, *200–201*, 1–9. https://doi.org/10.1016/j.pepi.2012.04.002

Evans, B. W. (2004). The serpentinite multisystem revisited: Chrysotile is metastable. *International Geology Review*, *46*(6), 479–506. https://doi.org/10.2747/0020-6814.46.6.479

Fry, B., McCurrach, S.-J., Gledhill, K., Power, W., Williams, M., Angove, M., et al. (2020). Sensor network warns of stealth tsunamis. *Eos*, *101*. https://doi.org/10.1029/2020eo144274

Funnell, M., Peirce, C., & Robinson, A. (2017). Structural variability of the Tonga-Kermadec forearc characterized using robustly constrained geophysical data. *Geophysical Journal International*, *210*(3), 1681–1702. https://doi.org/10.1093/gji/ggx260

Funnell, M. J., Peirce, C., Stratford, W. R., Paulatto, M., & Watts, A. B. (2013). Structure and deformation of the Tonga-Kermadec subduction system in the Louisville Ridge pre-collision zone. *AGU Fall Meeting Abstracts*, *2013*, T33A–T2614.

Gao, X., & Wang, K. (2014). Strength of stick-slip and creeping subduction megathrusts from heat flow observations. *Science*, *345*(6200), 1038–1041. https://doi.org/10.1126/science.1255487

Gerya, T. V., Connolly, J. A., Yuen, D. A., Gorczyk, W., & Capel, A. M. (2006). Seismic implications of mantle wedge plumes. *Physics of the Earth and Planetary Interiors*, *156*(1–2), 59–74. https://doi.org/10.1016/j.pepi.2006.02.005

GNS Science. (2020). NZ deep-ocean assessment and reporting of Tsunami (DART) data set [Dataset]. *GNS Science*. https://doi.org/10.21420/8TCZ-TV02?x=y

Goldstein, P., Dodge, D., Firpo, M., & Minner, L. (2003). SAC2000: Signal processing and analysis tools for seismologists and engineers. In W. H. K. Lee, H. Kanamori, P. C. Jennings, & C. Kisslinger (Eds.), *International handbook of earthquake and engineering seismology, Part B, International Geophysics Series* (Vol. 81, pp. 1613–1614). Academic Press.

Goswami, A., & Barbot, S. (2018). Slow-slip events in semi-brittle serpentinite fault zones. *Scientific Reports*, *8*(1), 6181. https://doi.org/10.1038/s41598-018-24637-z

Guillot, S., Schwartz, S., Reynard, B., Agard, P., & Prigent, C. (2015). Tectonic significance of serpentinites. *Tectonophysics*, *646*, 1–19. https://doi.org/10.1016/j.tecto.2015.01.020

Hartzell, S. H., & Heaton, T. H. (1983). Inversion of strong ground motion and teleseismic waveform data for the fault rupture history of the 1979 Imperial Valley California earthquake. *Bulletin of the Seismological Society of America*, *73*(6A), 1553–1583. https://doi.org/10.1785/bssa07306a1553

Hartzell, S. H., & Heaton, T. H. (1985). Teleseismic time functions for large, shallow subduction zone earthquakes. *Bulletin of the Seismological Society of America*, *75*, 965–1004.

Hayes, G. P., Moore, G. L., Portner, D. E., Hearne, M., Flamme, H., Furtney, M., & Smoczyk, G. M. (2018). Slab 2, a comprehensive subduction zone geometry model. *Science*, *362*(6410), 58–61. https://doi.org/10.1126/science.aat4723

Hirose, T., & Bystricky, M. (2007). Extreme dynamic weakening of faults during dehydration by coseismic shear heating. *Geophysical Research Letters*, *34*(14), L14311. https://doi.org/10.1029/2007gl030049

Houston, H., Anderson, H., Beck, S. L., Zhang, J., & Schwartz, S. (1993). The 1986 Kermadec earthquake and its relation to plate segmentation. *Pure and Applied Geophysics*, *140*(2), 331–364. https://doi.org/10.1007/bf00879411

Hyndman, R. D. (2007). The seismogenic zone of subduction thrust faults: What we know and don't know. In *The seismogenic zone of subduction thrust faults* (pp. 15–40). Columbia University Press.

Hyndman, R. D., & Peacock, S. M. (2003). Serpentinization of the forearc mantle. *Earth and Planetary Science Letters*, *212*(3–4), 417–432. https://doi.org/10.1016/s0012-821x(03)00263-2

Hyndman, R. D., Yamano, M., & Oleskevich, D. A. (1997). The seismogenic zone of subduction thrust faults. *Island Arc*, *6*(3), 244–260. https://doi.org/10.1111/j.1440-1738.1997.tb00175.x

Incorporated Research Institutions for Seismology (IRIS). (2025). IRIS Wilber 3 [Dataset]. http://ds.iris.edu/wilber3/find_event/

Intergovernmental Oceanographic Commission of UNESCO (IOC UNESCO). (2025). Sea level station monitoring facility [Dataset]. http://www.ioc-sealevelmonitoring.org

International Seismological Centre (ISC). (2025). International seismological centre [Dataset]. *ISC-EHB*. https://doi.org/10.31905/PY08W6S3

Kajiura, K. (1963). The leading wave of a tsunami. *Bulletin of the Earthquake Research Institute*, *41*(3), 535–571.

Kanamori, H., & Rivera, L. (2008). Source inversion of *W* phase: Speeding up seismic tsunami warning. *Geophysical Journal International*, *175*(1), 222–238. https://doi.org/10.1111/j.1365-246x.2008.03887.x

Kaproth, M., & Marone, C. (2013). Slow earthquakes, preseismic velocity changes, and the origin of slow frictional stick-slip. *Science*, *341*(6151), 1229–1232. https://doi.org/10.1126/science.1239577

Kikuchi, M., & Kanamori, H. (1991). Inversion of complex body waves-III. *Bulletin of the Seismological Society of America*, *81*(6), 2335–2350. https://doi.org/10.1785/bssa0810062335

Kitahara, S., Takenouchi, S., & Kennedy, G. C. (1966). Phase relations in the system MgO-SiO 2-H_2O at high temperatures and pressures. *American Journal of Science*, *264*(3), 223–233. https://doi.org/10.2475/ajs.264.3.223

Kohli, A. H., Goldsby, D. L., Hirth, G., & Tullis, T. (2011). Flash weakening of serpentinite at near-seismic slip rates. *Journal of Geophysical Research: Solid Earth*, *116*(B3), B03202. https://doi.org/10.1029/2010jb007833

Laske, G., Masters, G., Ma, Z., & Pasyanos, M. (2013). Update on CRUST1.0 – A 1-degree global model of Earth's crust. *Geophysical Research Abstracts*, *15*. Abstract EGU2013-2658.

Lay, T. (2018). A review of the rupture characteristics of the 2011 Tohoku-oki M_W 9.1 earthquake. *Tectonophysics*, *733*, 4–36. https://doi.org/10.1016/j.tecto.2017.09.022

Lay, T., Kanamori, H., Ammon, C. J., Koper, K. D., Hutko, A. R., Ye, L., et al. (2012). Depth-varying rupture properties of subduction zone megathrust faults. *Journal of Geophysical Research: Solid Earth*, *117*(B4), B04311. https://doi.org/10.1029/2011jb009133

Lay, T., Liu, C., & Kanamori, H. (2019). Enhancing tsunami warning using *P* wave coda. *Journal of Geophysical Research: Solid Earth*, *124*(10), 10583–10609. https://doi.org/10.1029/2019jb018221

Liu, S. M., Zhang, L., & He, C. R. (2023). Frictional properties of antigorite under high pore-fluid pressure and implications for slow-slip events in subduction zones. *Chinese Journal of Geophysics*, *66*(4), 1334–1347.

Lundgren, P. R., Okal, E. A., & Wiens, D. A. (1989). Rupture characteristics of the 1982 Tonga and 1986 Kermadec earthquakes. *Journal of Geophysical Research: Solid Earth*, *94*(B11), 15521–15539. https://doi.org/10.1029/jb094ib11p15521

Lythgoe, K., Bradley, K., Zeng, H., & Wei, S. (2023). Persistent asperities at the Kermadec subduction zone controlled by changes in forearc structure: 1976 and 2021 doublet earthquakes. *Earth and Planetary Science Letters*, *624*, 118465. https://doi.org/10.1016/j.epsl.2023.118465

Macías, J., Castro, M. J., Ortega, S., Escalante, C., & González-Vida, J. M. (2017). Performance benchmarking of Tsunami-HySEA model for NTHMP's inundation mapping activities. *Pure and Applied Geophysics*, *174*(8), 3147–3183. https://doi.org/10.1007/s00024-017-1583-1

McCann, W. R., Nishenko, S. P., Sykes, L. R., & Krause, J. (1979). Seismic gaps and plate tectonics: Seismic potential for major boundaries. *Pure and Applied Geophysics*, *117*, 1082–1147. https://doi.org/10.1007/978-3-0348-6430-5_2

Meng, Q., Heeszel, D. S., Ye, L., Lay, T., Wiens, D. A., Jia, M., & Cummins, P. R. (2015). The 3 May 2006 (M_W 8.0) and 19 March 2009 (M_W 7.6) Tonga earthquakes: Intraslab compressional faulting below the megathrust. *Journal of Geophysical Research: Solid Earth*, *120*(9), 6297–6316. https://doi.org/10.1002/2015jb012242

Mignan, A. (2014). The debate on the prognostic value of earthquake foreshocks: A meta-analysis. *Scientific Reports*, *4*(1), 4099. https://doi.org/10.1038/srep04099

Moore, D. E., & Lockner, D. A. (2007). Comparative deformation behavior of minerals in serpentinized ultramafic rock: Application to the slab-mantle interface in subduction zones. *International Geology Review*, *49*(5), 401–415. https://doi.org/10.2747/0020-6814.49.5.401

Moore, D. E., Lockner, D. A., Shengli, M., Summers, R., & Byerlee, J. D. (1987). Strengths of serpentinite gouges at elevated temperatures. *Journal of Geophysical Research: Solid Earth*, *102*, 14787–14801.

Mousavi, S. M., Ellsworth, W. L., Zhu, W., Chuang, L. Y., & Beroza, G. C. (2020). Earthquake transformer—An attentive deep-learning model for simultaneous earthquake detection and phase picking. *Nature Communications*, *11*(1), 3952. https://doi.org/10.1038/s41467-020-17591-w

Müller, R. D., Sdrolias, M., Gaina, C., & Roest, W. R. (2008). Age, spreading rates, and spreading asymmetry of the world's ocean crust. *Geochem.Geophys.Geosyst.*, *9*(4), Q04006. https://doi.org/10.1029/2007gc001743

Nevada Geodetic Laboratory. (2025). Geodetic data product [Dataset]. http://geodesy.unr.edu/NGLStationPages/stations/RAUL.sta

Nishenko, S. P. (1991). Circum-Pacific seismic potential: 1989-1999. *Pure and Applied Geophysics*, *135*(2), 169–259. https://doi.org/10.1007/bf00880240

Okada, Y. (1985). Surface deformation due to shear and tensile faults in a half-space. *Bulletin of the Seismological Society of America*, *75*(4), 1135–1154. https://doi.org/10.1785/bssa0750041135

Okal, E. A., Borrero, J. C., & Chagué-Goff, C. (2011). Tsunamigenic predecessors to the 2009 Samoa earthquake. *Earth-Science Reviews*, *107*(1–2), 128–140. https://doi.org/10.1016/j.earscirev.2010.12.007

Okazaki, K., & Katayama, I. (2014). Slow stick-slip of antigorite serpentinite under hydrothermal conditions as a possible mechanism for slow earthquakes. *Geophysical Research Letters*, *42*(4), 1099–1104. https://doi.org/10.1002/2014gl062735

Oleskevich, D. A., Hyndman, R. D., & Wang, K. (1999). The updip and downdip limits to great subduction earthquakes: Thermal and structural models of Cascadia, south Alaska, SW Japan, and Chile. *Journal of Geophysical Research: Solid Earth*, *104*(B7), 14965–14991. https://doi.org/10.1029/1999jb900060

Peacock, S. M. (1993). Metamorphism, dehydration, and the importance of the blueschist-eclogite transition in subducting oceanic crust. *Geological Society of America Bulletin*, *105*(5), 684–694. https://doi.org/10.1130/0016-7606(1993)105<0684:tiobed>2.3.co;2

Peacock, S. M., & Hyndman, R. D. (1999). Hydrous minerals in the mantle wedge and the maximum depth of subduction thrust earthquakes. *Geophysical Research Letters*, *26*(16), 2517–2520. https://doi.org/10.1029/1999gl900558

Pelletier, B., & Louat, R. (1989). Seismotectonics and present-day relative plate motions in the Tonga-Lau and Kermadec-Havre region. *Tectonophysics*, *165*(1–4), 237–250. https://doi.org/10.1016/0040-1951(89)90049-8

Power, W., Wallace, L., Wang, X., & Reyners, M. (2012). Tsunami hazard posed to New Zealand by the Kermadec and southern New Hebrides subduction margins: An assessment based on plate boundary kinematics, interseismic coupling and historical seismicity. *Pure and Applied Geophysics*, *169*(1–2), 1–36. https://doi.org/10.1007/s00024-011-0299-x

Proctor, B., & Hirth, G. (2016). "Ductile to brittle" transition in thermally stable antigorite gouge at mantle pressures. *Journal of Geophysical Research: Solid Earth*, *121*(3), 1652–1663. https://doi.org/10.1002/2015jb012710

Proctor, B. P., Mitchell, T. M., Hirth, G., Goldsby, D., Zorzi, F., Platt, J. D., & Di Toro, G. (2014). Dynamic weakening of serpentinite gouge and bare surfaces at seismic slip rates. *Journal of Geophysical Research: Solid Earth*, *119*(11), 8107–8131. https://doi.org/10.1002/2014jb011057

Reinen, L. A., Weeks, J. D., & Tullis, T. E. (1994). The frictional behavior of lizardite and antigorite serpentinites: Experiments, constitutive models, and implications for natural faults. *Pure and Applied Geophysics*, *143*(1–3), 317–358. https://doi.org/10.1007/bf00874334

Reynard, B. (2013). Serpentine in active subduction zones. *Lithos*, *178*, 171–185. https://doi.org/10.1016/j.lithos.2012.10.012

Romano, F., Lorito, S., Lay, T., Piatanesi, A., Volpe, M., Murphy, S., & Tonini, R. (2020). Benchmarking the optimal time alignment of tsunami waveforms in nonlinear joint inversions for the M_W 8.8 2010 Maule (Chile) earthquake. *Frontiers of Earth Science*, *8*. https://doi.org/10.3389/feart.2020.585429

Romano, F., Piatanesi, A., Lorito, S., & Hirata, K. (2010). Slip distribution of the 2003 Tokachi-oki M_W 8.1 earthquake from joint inversion of tsunami waveforms and geodetic data. *Journal of Geophysical Research: Solid Earth*, *115*(B11), B11313. https://doi.org/10.1029/2009jb006665

Romano, F., Piatanesi, A., Lorito, S., Tolomei, C., Atzori, S., & Murphy, S. (2016). Optimal time alignment of tide-gauge tsunami waveforms in nonlinear inversions: Application to the 2015 Illapel (Chile) earthquake. *Geophysical Research Letters*, *43*(21), 11226–11235. https://doi.org/10.1002/2016gl071310

Romano, F. R., Gusman, A. R., Power, W., Piatanesi, A., Volpe, M., Scala, A., & Lorito, S. (2021). Tsunami source of the 2021 M_W8.1 Raoul Island earthquake from DART and tide-gauge data inversion. *Geophysical Research Letters*, *48*(17), e2021GL094449. https://doi.org/10.1029/2021gl094449

Schmidt, M. W., & Poli, S. (1998). Experimentally based water budgets for dehydrating slabs and consequences for arc magma generation. *Earth and Planetary Science Letters*, *163*(1–4), 361–379. https://doi.org/10.1016/s0012-821x(98)00142-3

Schwartz, S., Guillot, S., Reynard, B., Lafay, R., Debret, B., Nicollet, C., et al. (2013). Pressure–temperature estimates of the lizardite/antigorite transition in high pressure serpentinites. *Lithos*, *178*, 197–210. https://doi.org/10.1016/j.lithos.2012.11.023

Sladen, A., & Trevisan, J. (2018). Shallow megathrust earthuake ruptures betrayed by their outr-trench aftershock signature. *Earth and Planetary Science Letters*, *483*, 105–113. https://doi.org/10.1016/j.epsl.2017.12.006

Szwillus, W., Afonso, J. C., Ebbing, J., & Mooney, W. D. (2019). Global crustal thickness and velocity structure from geostatistical analysis of seismic data. *Journal of Geophysical Research: Solid Earth*, *124*(2), 1626–1652. https://doi.org/10.1029/2018jb016593

Takahashi, M., Uehara, S.-I., Mizoguchi, K., Shimizu, I., Okazaki, K., & Masuda, K. (2011). On the transient response of serpentine (antigorite) gouge to stepwise changes in slip velocity under high-temperature conditions. *Journal of Geophysical Research: Solid Earth*, *116*(B10), B10405. https://doi.org/10.1029/2010jb008062

Todd, E. K., & Lay, T. (2013). The 2011 Northern Kermadec earthquake doublet and subduction zone faulting interactions. *Journal of Geophysical Research: Solid Earth*, *118*(1), 249–261. https://doi.org/10.1029/2012jb009711

Tontini, F. C., Bassett, D., de Ronde, C. E. J., Timm, C., & Wysoczanski, R. (2019). Early evolution of a young back-arc basin in the Havre Trough. *Nature Geoscience*, *12*, 856–862.

U.S. Geological Survey (USGS). (2025). Search earthquake catalog [Dataset]. https://earthquake.usgs.gov/earthquakes/search/

Wada, I., & Wang, K. (2009). Common depth of slab-mantle decoupling: Reconciling diversity and uniformity of subduction zones. *Geochemistry, Geophysics, Geosystems*, *10*, Q10009. https://doi.org/10.1029/2009gc002570

Wallace, L. M., Ellis, S., & Mann, P. (2009). Collisional model for rapid fore-arc block rotations, arc curvature, and episodic back-arc rifting in subduction settings. *Geochemistry, Geophysics, Geosystems*, *10*(5), Q05001. https://doi.org/10.1029/2008gc002220

Wang, K., Huang, T., Tilmnn, F., Peacock, S. M., & Lange, D. (2020). Role of serpentinized mantle wedge in affecting megathrust seismogenic behavior in the area of the 2010 M=8.8 Maule earthquake. *Geophysical Research Letters*, *47*(22), e2020GL090482. https://doi.org/10.1029/2020gl090482

Wang, K., Luo, H., He, J., & Carvajal, M. (2025). Soft barrier to megathrust rupture enabled by serpentinized mantle wedge: The Chile subduction zone. *Earth and Planetary Science Letters*, *650*, 119115. https://doi.org/10.1016/j.epsl.2024.119115

Wang, Y., Heidarzadeh, M., Satake, K., & Hu, G. (2022). Characteristics of two tsunamis generated by successive M_W 7.4 and M_W 8.1 earthquakes in the Kermadec Islands on 4 March 2021. *Natural Hazards and Earth System Sciences*, *22*(3), 1073–1082. https://doi.org/10.5194/nhess-22-1073-2022

Watada, S., Kusumoto, S., & Satake, K. (2014). Traveltime delay and initial phase reversal of distant tsunamis coupled with the self-gravitating elastic Earth. *Journal of Geophysical Research: Solid Earth*, *119*(5), 4287–4310. https://doi.org/10.1002/2013jb010841

Wessel, P., Luis, J. F., Uieda, L., Scharroo, R., Wobbe, F., Smith, W. H. F., & Tian, D. (2019). The generic mapping tools version 6. *Geochemistry, Geophysics, Geosystems*, *20*(11), 5556–5564. https://doi.org/10.1029/2019gc008515

Wetzler, N., Lay, T., Brodsky, E. E., & Kanamori, H. (2017). Rupture-depth-varying seismicity patterns for major and great ($M_W \geq 7.0$) megathrust earthquakes. *Geophysical Research Letters*, *44*(19), 9663–9671. https://doi.org/10.1002/2017gl074573

Wetzler, N., Lay, T., Brodsky, E. E., & Kanamori, H. (2018). Systematic deficiency of aftershocks in areas of high coseismic slip for large subduction zone earthquakes. *Science Advances*, *4*(2), eaao3225. https://doi.org/10.1126/sciadv.aao3225

Ye, L., Bai, Y., Si, D., Lay, T., Cheung, K. F., & Kanamori, H. (2022). Rupture model for the 29 July 2021 M_W 8.2 Chignik, Alaska Earthquake constrained by seismic, geodetic, and tsunami observations. *Journal of Geophysical Research: Solid Earth*, e2021JB023676. https://doi.org/10.1029/2021JB023676

Ye, L., Kanamori, H., Avouac, J. P., Li, L., Cheung, K. F., & Lay, T. (2016). The 16 April 2016, M_W 7.8 (M_S 7.5) Ecuador earthquake: A quasi-repeat of the 1942 M_S 7.5 earthquake and partial re-rupture of the 1906 M_S 8.6 Colombia–Ecuador earthquake. *Earth and Planetary Science Letters*, *454*, 248–258. https://doi.org/10.1016/j.epsl.2016.09.006

Ye, L., Lay, T., & Kanamori, H. (2012). Intraplate and interplate faulting interactions during the August 31, 2012, Philippine Trench earthquake (Mw 7.6) sequence. *Geophysical Research Letters*, *39*(24). https://doi.org/10.1029/2012gl054164

Ye, L., Lay, T., & Kanamori, H. (2021). The 25 March 2020 M_W 7.5 Paramushir, northern Kuril Islands earthquake and major ($M_W \geq 7.0$) near-trench intraplate compressional faulting. *Earth and Planetary Science Letters*, *556*, 115728.

Ye, L., Lay, T., Kanamori, H., & Rivera, L. (2016). Rupture characteristics of major and great ($M_W \geq 7.0$) megathrust earthquakes from 1990-2015: 1. Source parameter scaling relationships. *Journal of Geophysical Research: Solid Earth*, *121*(2), 826–844. https://doi.org/10.1002/2015jb012426

Ye, L., Lay, T., Kanamori, H., Yamazaki, Y., & Cheung, K. F. (2021). The 22 July 2020 M_W 7.8 Shumagin seismic gap earthquake: Partial rupture of a weakly coupled megathrust. *Earth and Planetary Science Letters*, *562*, 116879. https://doi.org/10.1016/j.epsl.2021.116879

Zeng, H., Wei, S., & Yang, H. (2025). The 2021 Mw8.1 Kermadec megathrust earthquake: An event rupturing the slab-mantle interface with up-dip high-frequency seismic energy radiation. *Geophysical Research Letters*, *52*(4), e2024GL113015. https://doi.org/10.1029/2024gl113015

AGU PUBLICATIONS

Journal of Geophysical Research – Solid Earth

Supporting Information for

The 2021 M_W 8.1 Kermadec Earthquake Sequence: Great Earthquake Rupture along the Mantle/Slab Contact

Lingling Ye[a,*], Yangming Hu[a], Tao Xia[a], Thorne Lay[b], Yingquan Sang[a,c], Xiaofei Chen[a], Hiroo Kanamori[d], Fabrizio Romano[e], Stefano Lorito[e], and Zhou Gui[f]

[a] *Department of Earth and Space Sciences, Southern University of Science and Technology, Shenzhen, 518055, China*

[b] *Department of Earth and Planetary Sciences, University of California Santa Cruz, Santa Cruz, CA 95064, USA*

[c] *Institute of Geology and Geophysics, Chinese Academy of Sciences, Beijing, 100029, China*

[d] *Seismological Laboratory, California Institute of Technology, Pasadena, CA 91125, USA*

[e] *Istituto Nazionale di Geofisica e Vulcanologia, Roma, Italy*

[f] *Institute of Oceanology Chinese Academy of Sciences, Qingdao, 266071, China*

* Corresponding author: Lingling Ye; E-mail address: yell@sustech.edu.cn

Contents of this file

Figures S1 to S16. Tables S1 and S2.

Introduction

We provide supplemental figures and tables of the material presented in the main text. Specifically,

Figure S1. The historical distribution of large earthquakes along the Tonga-Kermadec subduction zone from the USGS-NEIC ($M_W \geq 7.0$) and the GCMT ($M_W \geq 6.9$) catalogs.

Figure S2. Details of the of 2021 Kermadec sequence from the USGS-NEIC and GCMT catalogs, including the prior large earthquake distribution.

Figure S3. The distribution of shallow GCMT mechanisms from 1976-2023 for northern Kermadec.

Figure S4. The detailed geometry of the rupture model grid used for finite-fault inversions for the 2021 foreshock and mainshock.

Figure S5. The finite-fault inversion of teleseismic and geodetic data for the M_W 7.4 foreshock.

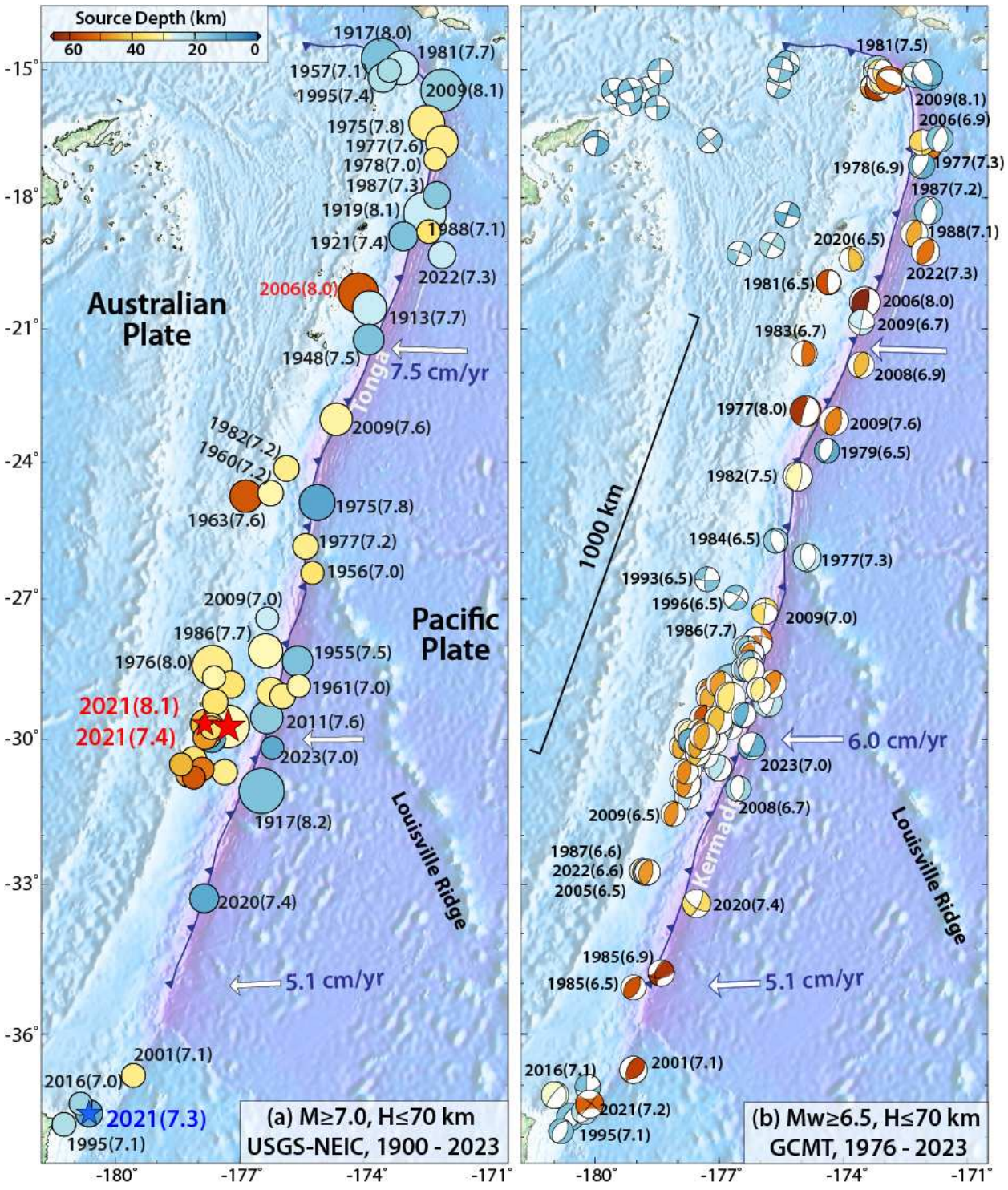

Figure S1. Large shallow earthquakes along the Tonga-Kermadec subduction zone. (a) Epicenters of *M*7+ earthquakes from the USGS-NEIC catalog from 1900 to 2023, scaled proportionally to magnitude and color-coded by source depth. The year and estimated magnitude are indicated for many events. Blue and red stars show the epicenters of three major Kermadec earthquakes in 2021. Vectors indicate motion of the Pacific Plate relative to the Australian Plate. (b) *M*6.5+ earthquake focal mechanisms from the GCMT catalog from 1976 to 2023, scaled proportionally to magnitude, color-coded by source depth, and plotted at the GCMT centroid locations. The year and M_W are indicated for many events.

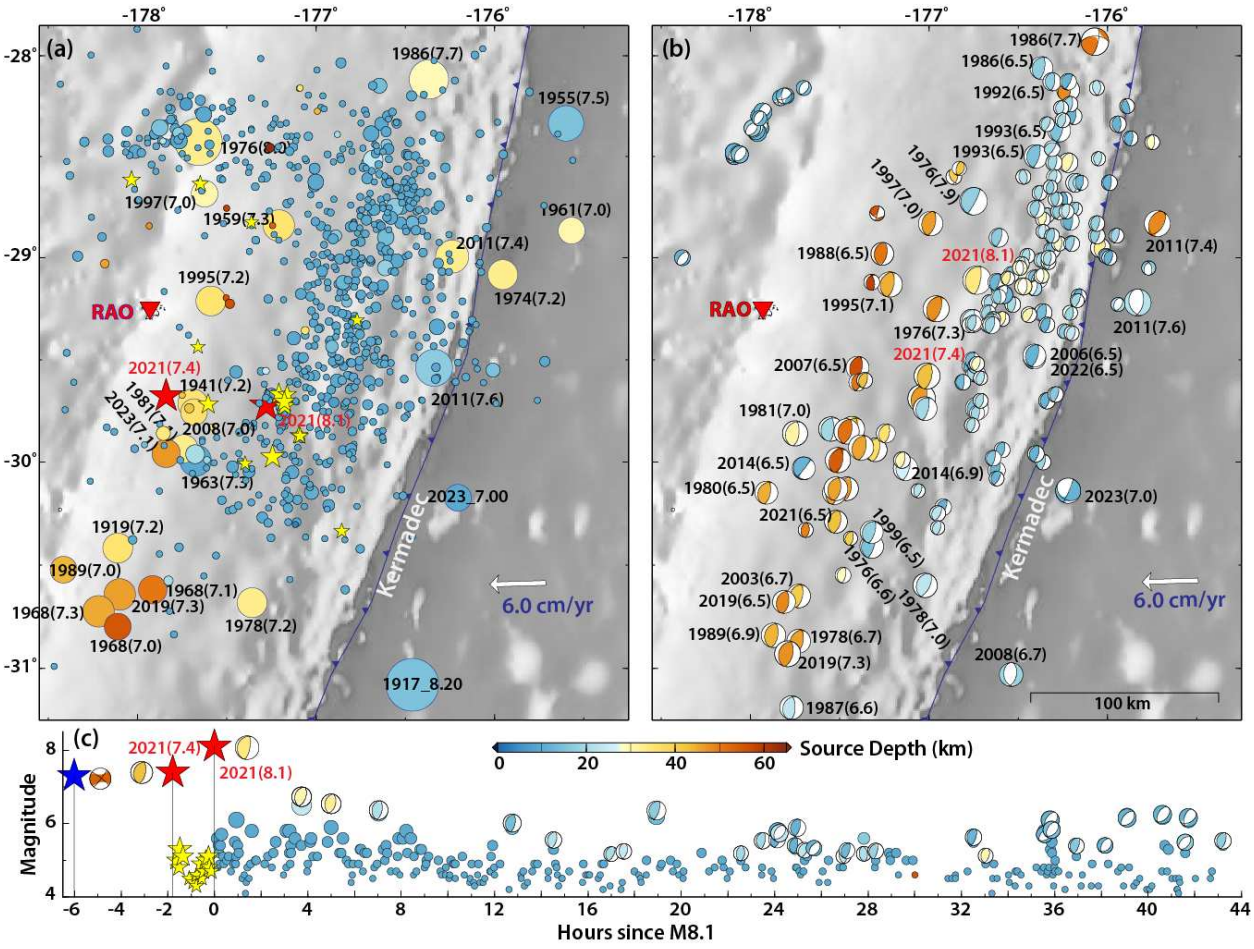

Figure S2. Spatial and temporal distribution of the 2021 M_W 8.1 Kermadec earthquake sequence. (a) The NEIC-USGS epicenters for M4.5+ events are shown with yellow stars at epicenters of events between the M_W 7.4 and M_W 8.1 events and small blue circles for aftershocks within 60 days after the M_W 8.1 mainshock. Historical M7.0+ earthquake epicenters are indicated by large circles scaled proportionally to magnitude and color-coded by source depth, with year and estimated magnitude labeled. (b) GCMT focal mechanisms scaled proportionally to magnitude and plotted at their centroid locations for 60-day aftershocks and large historical earthquakes in the region with M6.5+ with year and M_W labeled. (c) Earthquake magnitude time sequence along the source region in (a) and (b) for the 2021 northern Kermadec sequence. Major events in the sequence are highlighted with the red stars with GCMT focal mechanisms, yellow stars indicate the events between the 2021 M_W 7.4 and M_W 8.1 events, while blue circles are for early aftershocks of the M_W 8.1 event. Symbols are color coded by source depth.

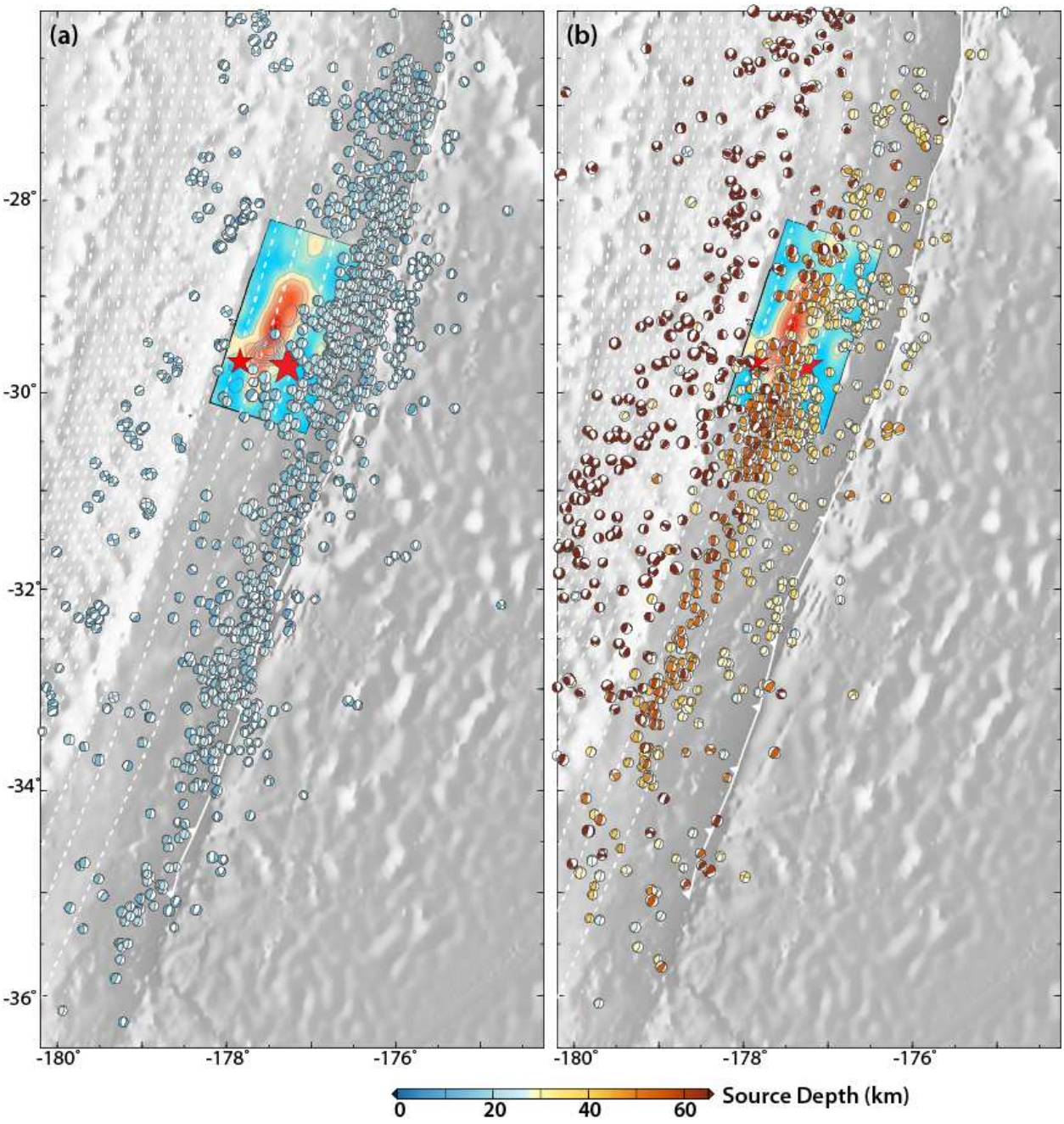

Figure S3. Focal mechanisms for earthquakes with the depth < 70 km along the Tonga-Kermadec subduction zone from the GCMT catalog from 1976-2023. (a) Focal mechanisms for earthquakes with centroid depth less 25 km. (b) Focal mechanisms for earthquakes with centroid depths from 25 - 70 km. Focal mechanisms are scaled proportionally to magnitude, color-coded by source depth, and plotted at the GCMT centroid locations. Red stars indicate the hypocentral locations for the 2021 M_W 7.4 and M_W 8.1 events, along with the mainshock slip distributions (Figure 4).

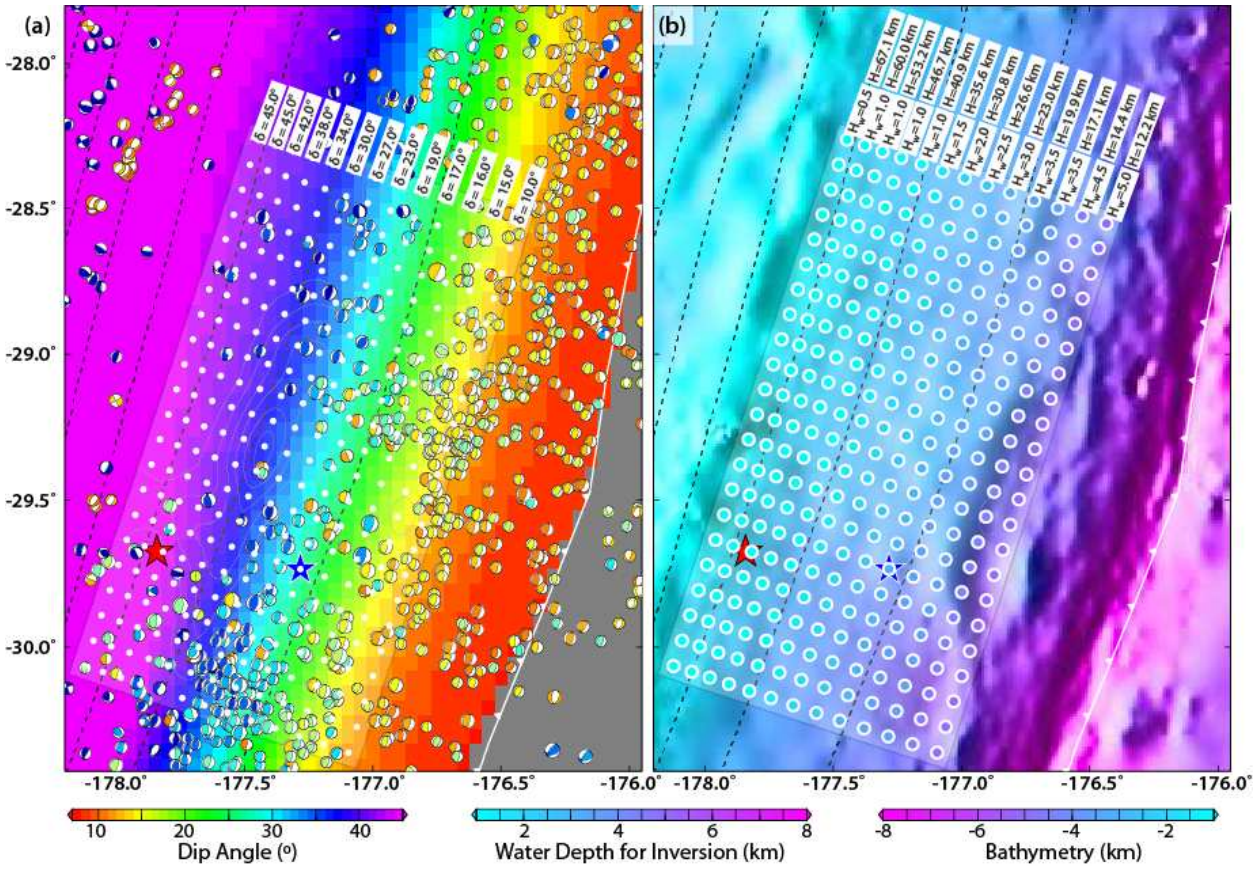

Figure S4. **Geometry of the rupture model surface (grid) as adapted from the SLAB2 model of the Pacific-Australian plate boundary interface.** Color pattern in (a) indicates the dip of the interface in the SLAB2 model with dashed lines indicating 20 km depth intervals along the interface. All GCMT mechanisms from 1976 to 2021 are shown at their centroid locations. The gridded box indicates the fault model surface along which the dip (δ) for each along-dip row varies with the indicated values. The red and blue stars denote the hypocenter of the 2021 M_W 7.4 foreshock and the 2021 M_W 8.1 mainshock, respectively. (b) The depth below sea surface (H) of each row of the grid, with the water depths (H_w) used in local 1D velocity model computations for each row being adapted from the regional bathymetry model. The overall fault representation is a 2.5D approximation of the SLAB2 model and bathymetry.

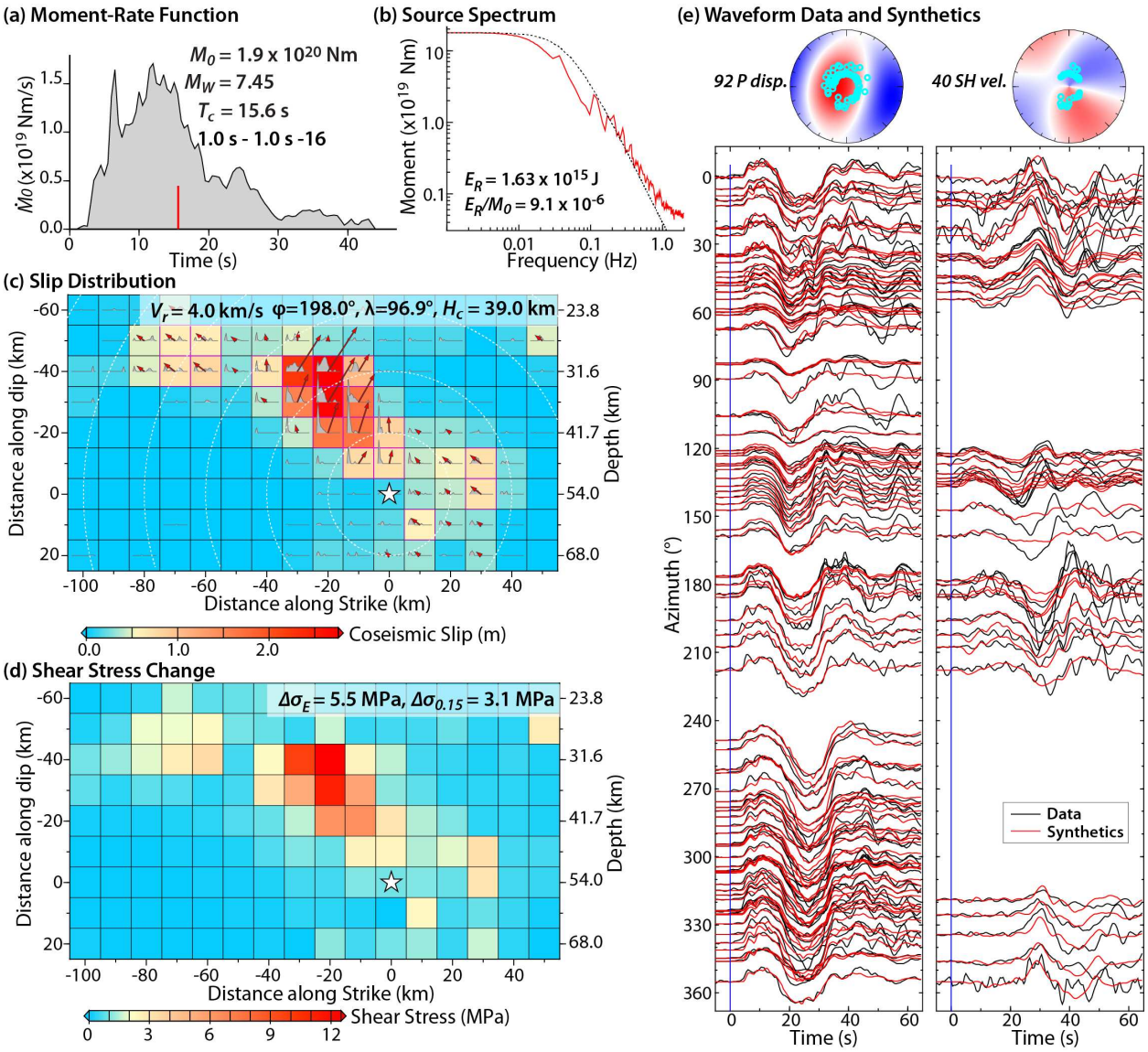

Figure S5. Source model obtained from joint inversion for the M_W 7.4 foreshock. (a) Moment-rate function indicating the seismic moment M_0, M_W, centroid time T_c, and subfault source time functions parameterized as 16 1.0-s rise time symmetric triangles offset by 1.0 s. (b) Source spectrum obtained from the moment rate function for frequencies <0.05 Hz and from stacks of radiation pattern and propagation corrected far-field *P* wave spectra for higher frequencies. E_R is the radiated seismic energy up to 1 Hz. (c) Spatial distribution of slip on the 2.5D fault model (see Figure S4), with the slip in each fault indicated by the color scale with red vectors indicating the subfault slip magnitude and direction, and the gray polygons indicating the subfault source time functions (shown in map view in Figure 4a). V_r is the imposed maximum allowed rupture velocity, and the white dashed circles indicate the position of the corresponding isochrones in 10 s intervals. White star indicates the hypocentral location. (d) Shear stress variations on the slip surface indicated by color scale. $\Delta\sigma_E$ is the slip-weighted static stress drop, and $\Delta\sigma_{0.15}$ is a circular crack stress drop for overall slip areas with more than 15% slip relative to peak subfault slip (following Ye et al., 2016). (e) Comparison of observed (black lines) and predicted (red lines) teleseismic *P* and *SH* waves, with the data distributions indicated by take-off angle and azimuth in the stereographic projections on the average source radiation patterns. GNSS observations and model predictions are shown in Figure 4a.

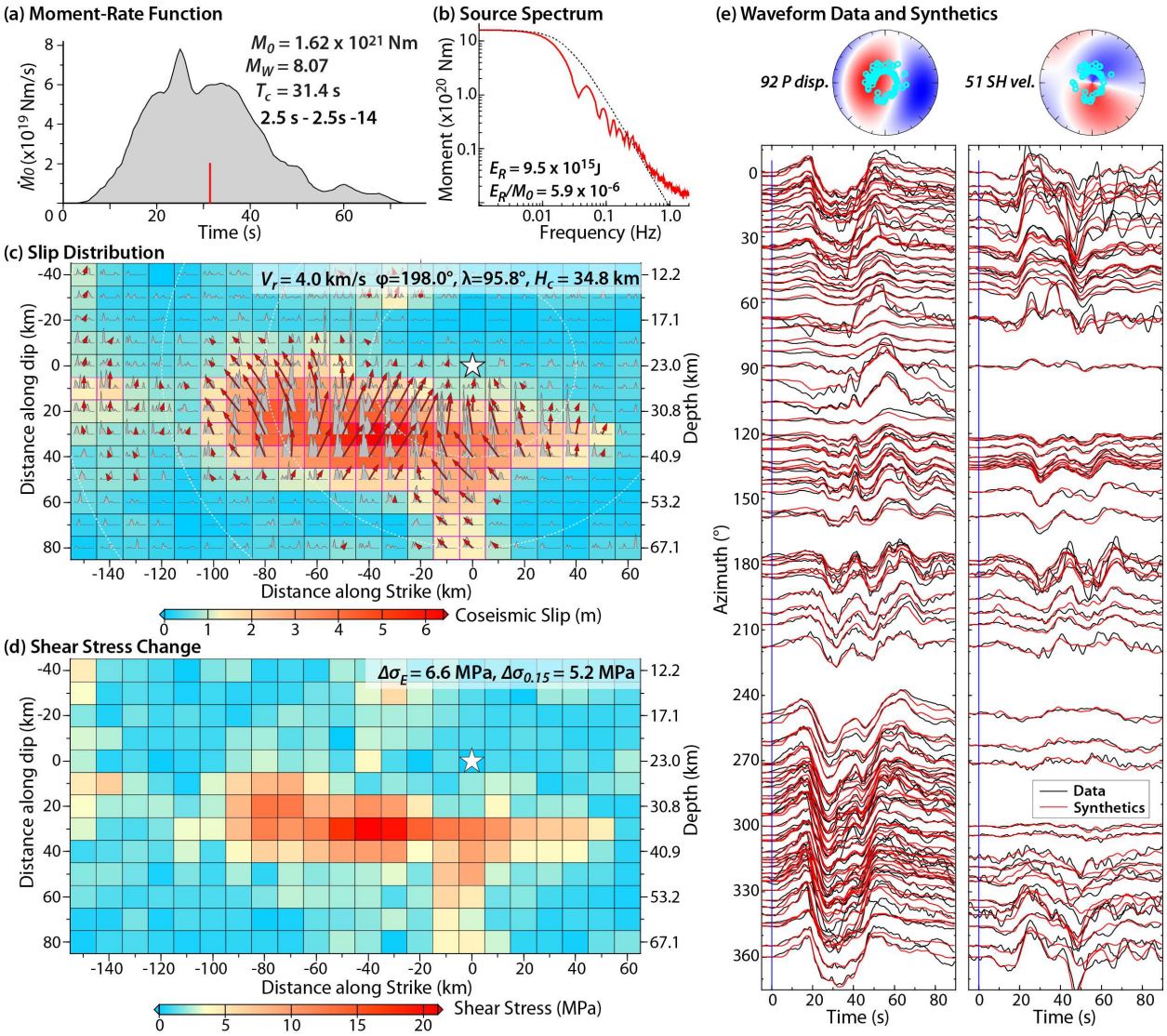

Figure S6. Source model obtained from joint inversion for the M_W 8.1 mainshock. (a) Moment-rate function indicating the seismic moment M_0, M_W, centroid time T_C, and subfault source time functions parameterized as 14 2.5-s rise time symmetric triangles offset by 2.5 s. (b) Source spectrum obtained from the moment rate function for frequencies less than 0.05 Hz and from stacks of radiation pattern and propagation corrected far-field *P* wave spectra for higher frequencies. E_R is the radiated seismic energy up to 1 Hz. (c) Spatial distribution of slip on the 2.5D fault model (see Figure S4), with the slip in each fault indicated by the color scale with red vectors indicating the subfault slip magnitude and direction, and the gray polygons indicating the subfault source time functions (shown in map view in Figure 4b). V_r is the imposed maximum allowed rupture velocity, and the white dashed circles indicate the position of the corresponding isochrones in 10 s intervals. White star indicates the hypocentral location. (d) Shear stress variations on the slip surface indicated by color scale. $\Delta\sigma_E$ is the slip-weighted static stress drop, and $\Delta\sigma_{0.15}$ is a circular crack stress drop for overall slip areas with more than 15% slip relative to peak subfault slip (following Ye et al., 2016). (e) Comparison of observed (black lines) and predicted (red lines) teleseismic *P* and *SH* waves, with the data distributions indicated by take-off angle and azimuth in the stereographic projections on the average source radiation patterns. GNSS observations and model predictions are shown in Figure 4b.

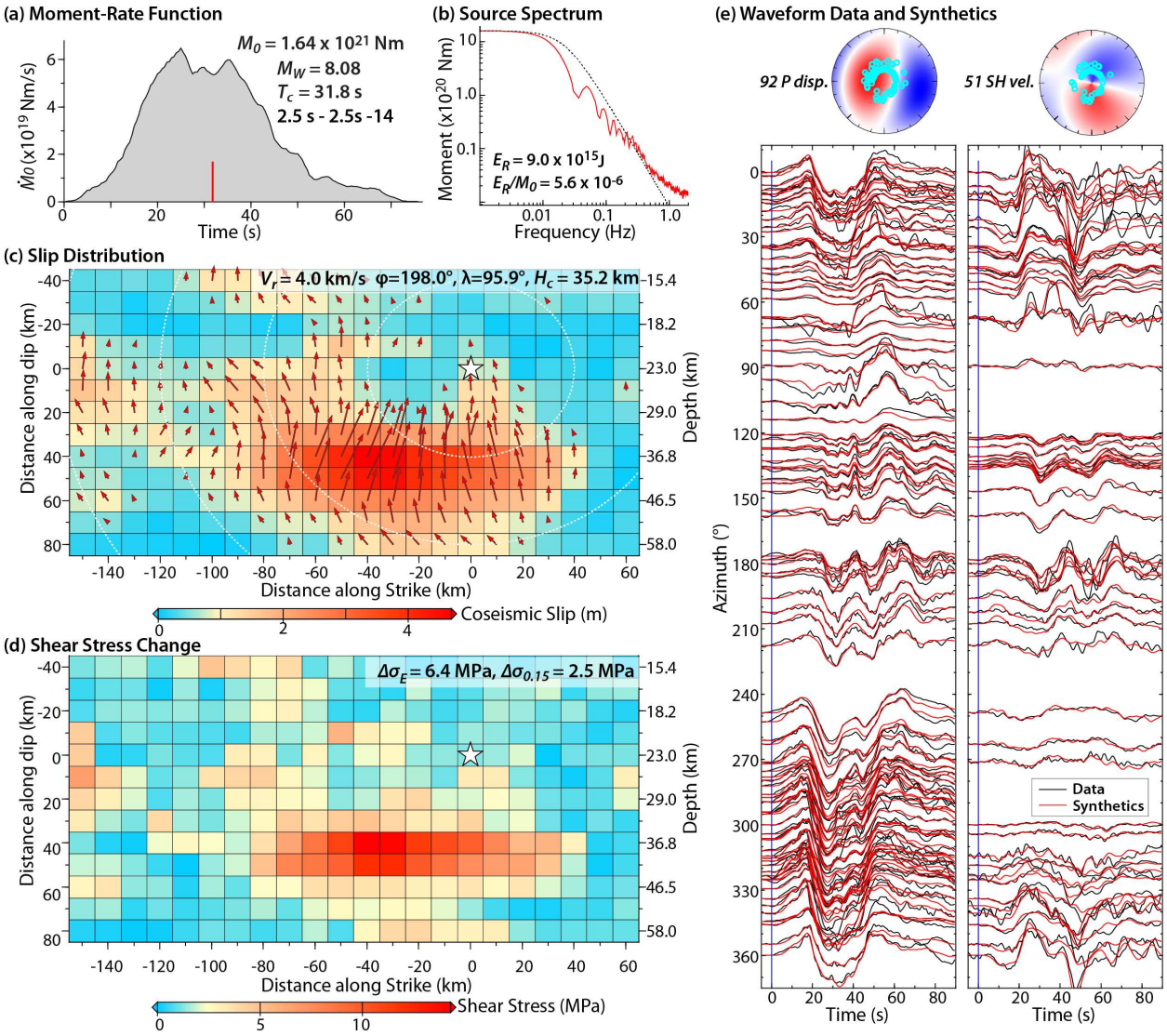

Figure S7. Source model obtained from inversion of only teleseismic body waves for the M_W 8.1 mainshock in the 2021 Northern Kermadec sequence. (a) Moment-rate function indicating the seismic moment M_0, M_W, centroid time T_C, and subfault source time functions parameterized as 14 2.5-s rise time symmetric triangles offset by 2.5 s. (b) Source spectrum obtained from the moment rate function for frequencies less than 0.05 Hz and from stacks of radiation pattern and propagation corrected far-field *P* wave spectra for higher frequencies. E_R is the radiated seismic energy up to 1 Hz. (c) Spatial distribution of slip on the 2.5D fault model (see Figure S4), with the slip in each fault indicated by the color scale with red vectors indicating the subfault slip magnitude and direction, and the gray polygons indicating the subfault source time functions. V_r is the imposed maximum allowed rupture velocity, and the white dashed circles indicate the position of the corresponding isochrones in 10 s intervals. White star indicates the hypocentral location. (d) Shear stress variations on the slip surface indicated by color scale. $\Delta\sigma_E$ is the slip-weighted static stress drop, and $\Delta\sigma_{0.15}$ is a circular crack stress drop for overall slip areas with more than 15% slip relative to peak subfault slip (following Ye et al., 2016a). (e) Comparison of observed (black lines) and predicted (red lines) teleseismic *P* and *SH* waves, with the data distributions indicated by take-off angle and azimuth in the stereographic projections on the average source radiation patterns.

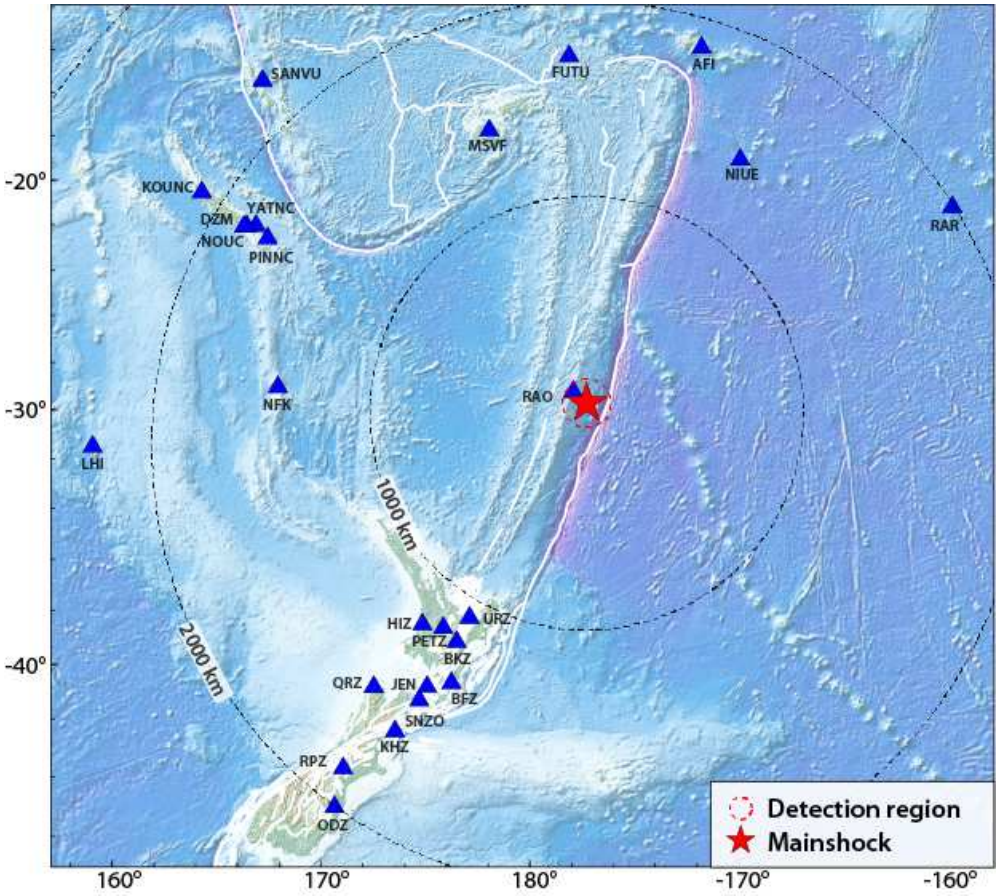

Figure S8. Source area and station distribution for detecting foreshocks between the M_W 7.4 foreshock and M_W 8.1 mainshock. The red star denotes the USGS-NEIC location for the M_W 8.1 mainshock, with the dashed red circle delineating the designated source-searching region.

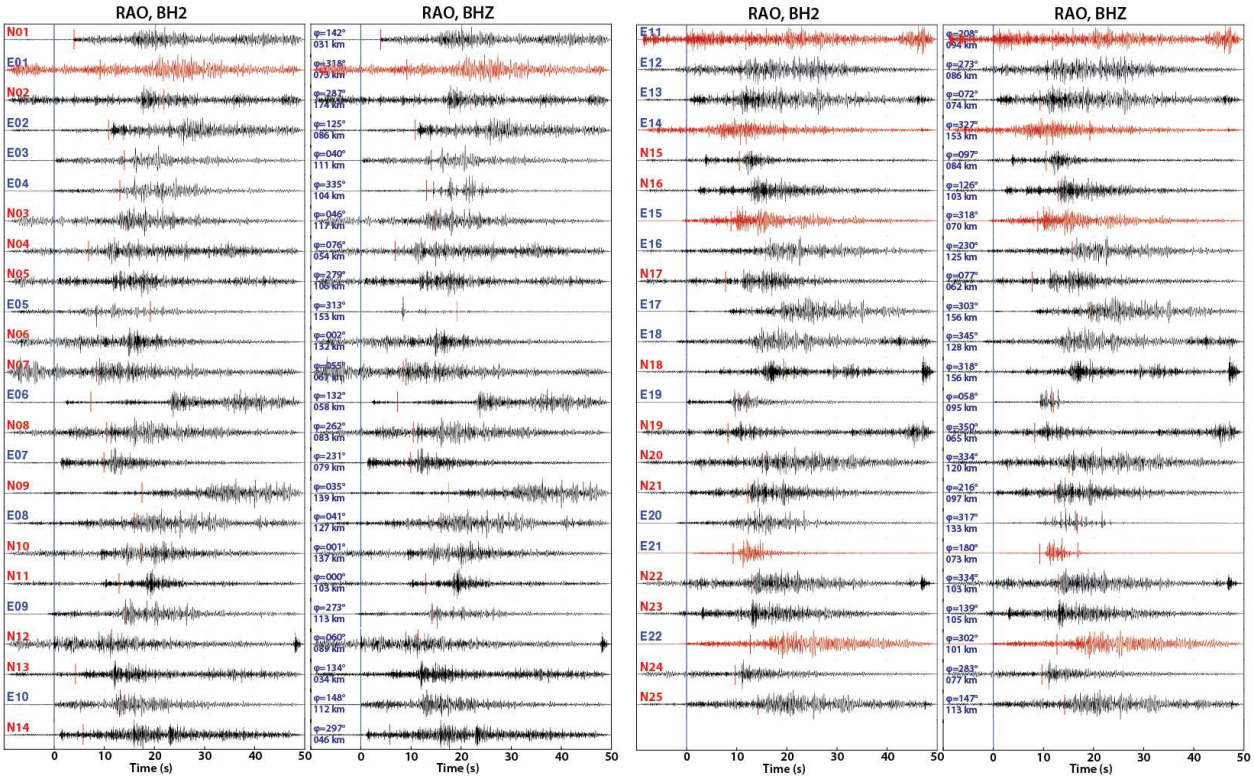

Figure S9. Seismic waveforms for 47 events occurring between the M_W 7.4 foreshock and M_W 8.1 mainshock recorded by the broadband seismic station RAO on Raoul Island. The black waveforms represent 41 foreshocks detected using the EQtransformer/REAL algorithms with stations outlined in Figure S8. Meanwhile, the red waveforms correspond to 6 foreshocks listed in the ISC catalog but not detected in our study. The labels E01-E22 are consistent with those in Figure 7 and Table S1, while N01-N25 denote newly detected events.

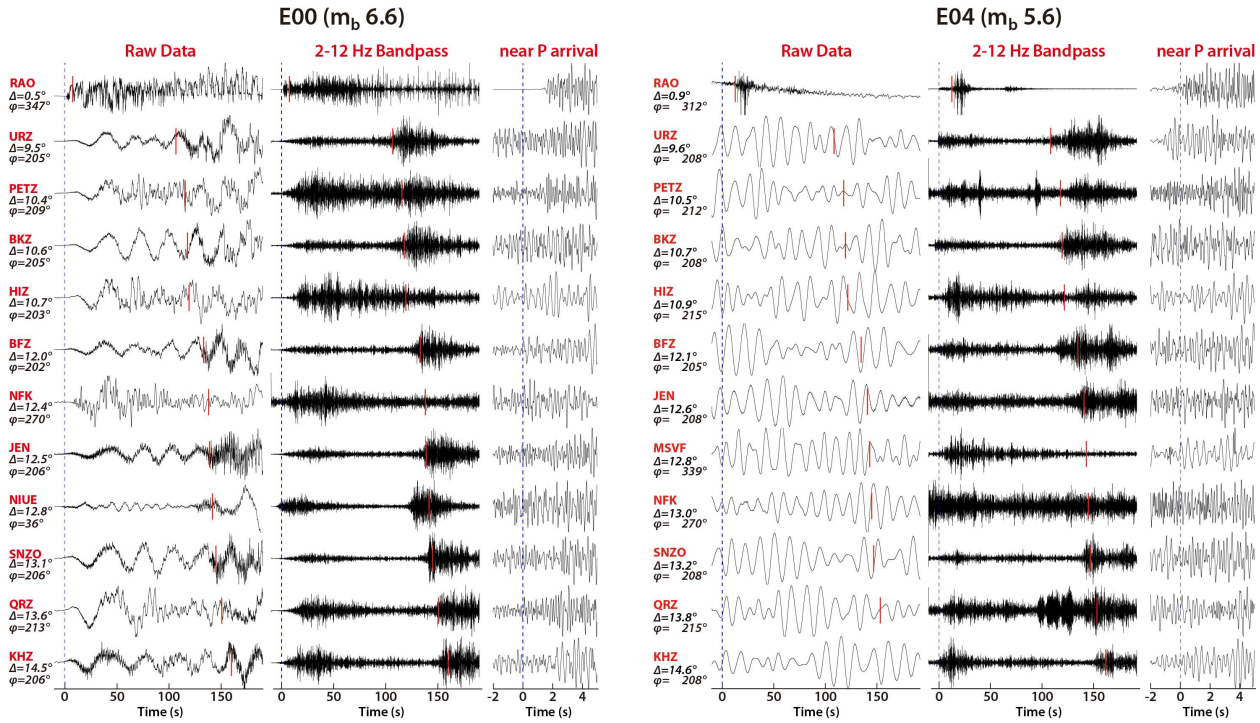

Figure S10. Seismic waveforms for the M_W 7.4 foreshock (E00, m_b = 6.6) and the second-largest foreshock E04 (m_b = 5.6), recorded by nearby broadband stations (Figure S8). Raw data and high-frequency bandpass-filtered data (2-12 Hz), accompanied by a zoom-in segment near the predicted *P* arrivals, are aligned with the predicted *P* arrivals (blue dashed line) based on the ISC location. Red bars indicate the corresponding predicted *S* arrivals; Δ and φ show the source-station distance and azimuth, respectively.

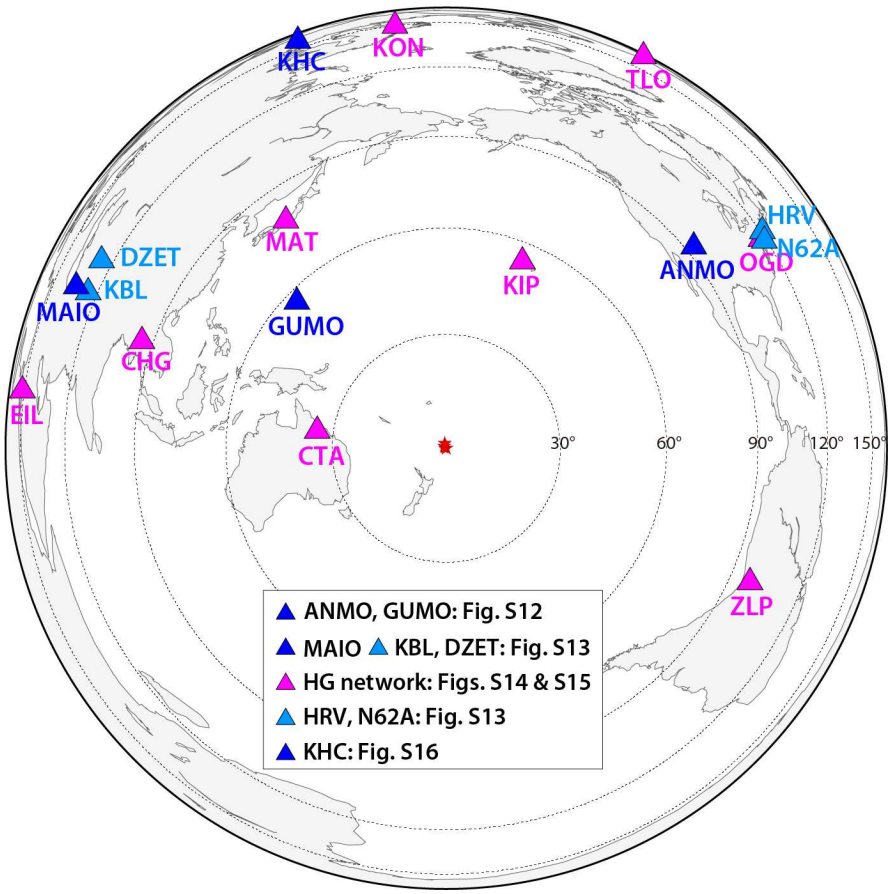

Figure S11. Station distribution of available digital seismic data for the 1976 major earthquakes. The red stars denote the epicenters of the 1976 and 2021 earthquakes. The light blue stations are stations recording the 2021 earthquakes that are not collocated with the stations recording the 1976 earthquakes.

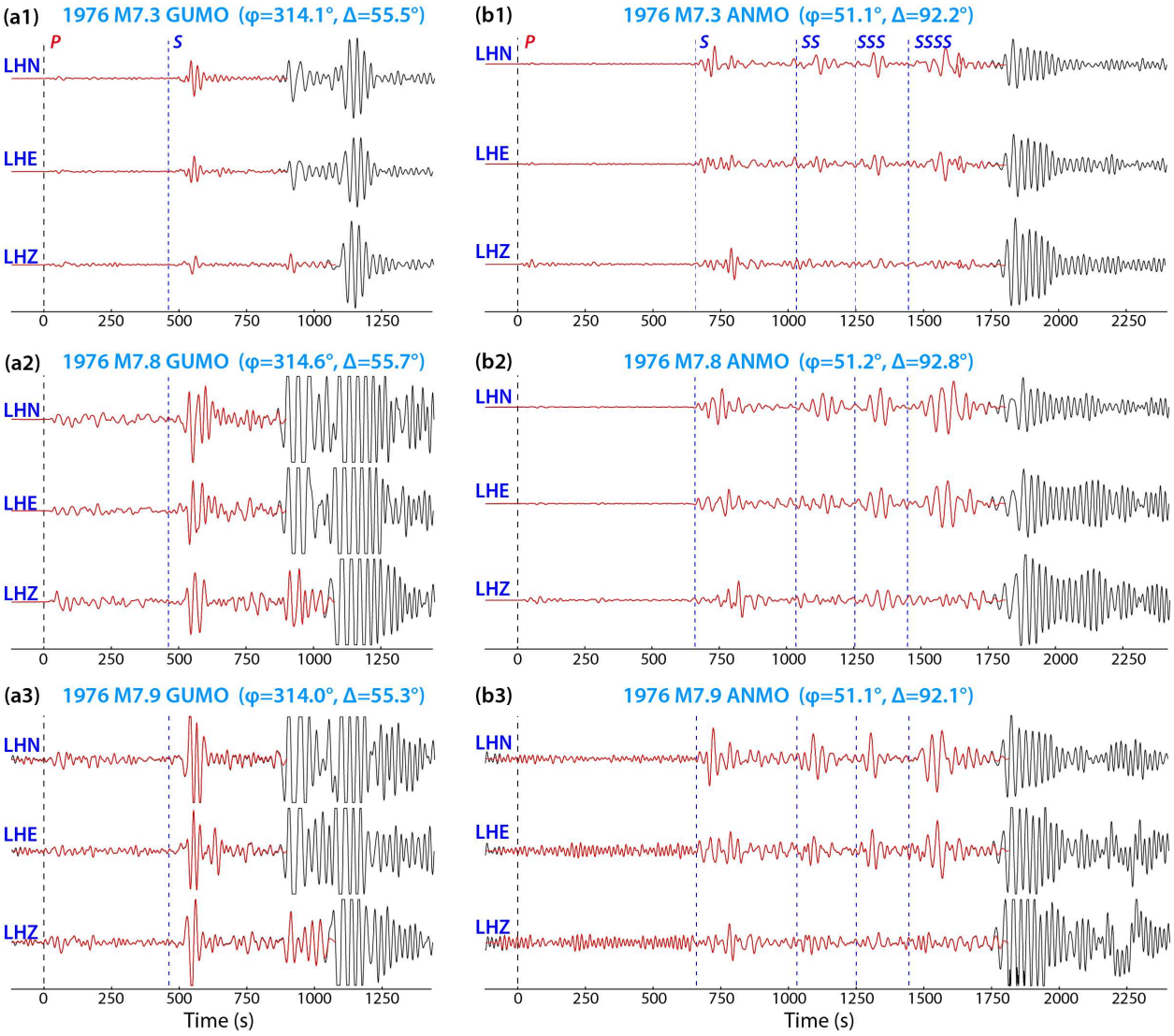

Figure S12. Comparisons of seismic waveforms between the raw data and the windowed data used in Figure 10 for the three major earthquakes in 1976 at stations GUMO and ANMO. The raw data are plotted in black, and the windowed, unclipped portions of the data are plotted in red. Data are aligned on *P* arrivals. The relative arrival times for *S*, *SS*, *SSS*, and *SSSS* phases predicted by the IASP91 model are labeled.

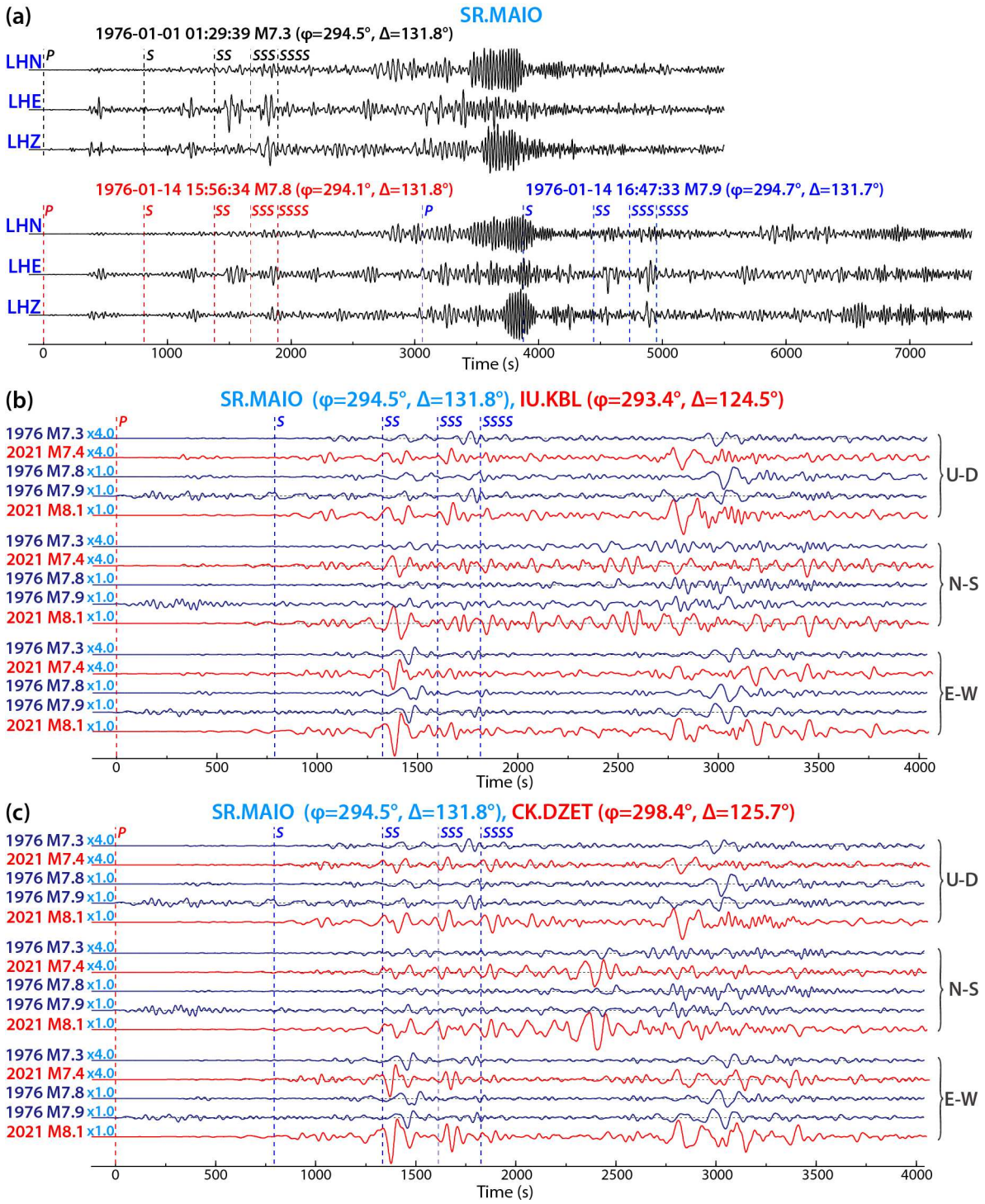

Figure S13. Comparisons of seismic waveforms between the 1976 and 2021 major earthquakes at stations MAIO, KBL and DZET. Panel (a) shows raw seismic waveforms of the 1976 earthquakes at station SR.MAIO. Note that the waveforms of the M7.8 and M7.9 events overlap as they occurred 51 minutes apart. In panels (b) and (c), seismic waveforms at KBL and DZET for the 2021 earthquakes are compared with waveforms of station SR.MAIO for the 1976 earthquakes. Records are filtered in the period band 30-150 sec. DZET is ~868 km from MAIO. KBL is ~886 km from MAIO. Data are aligned on *P* arrivals. The relative arrival times for *S*, *SS*, *SSS*, and *SSSS* phases predicted by the IASP91 model are labeled.

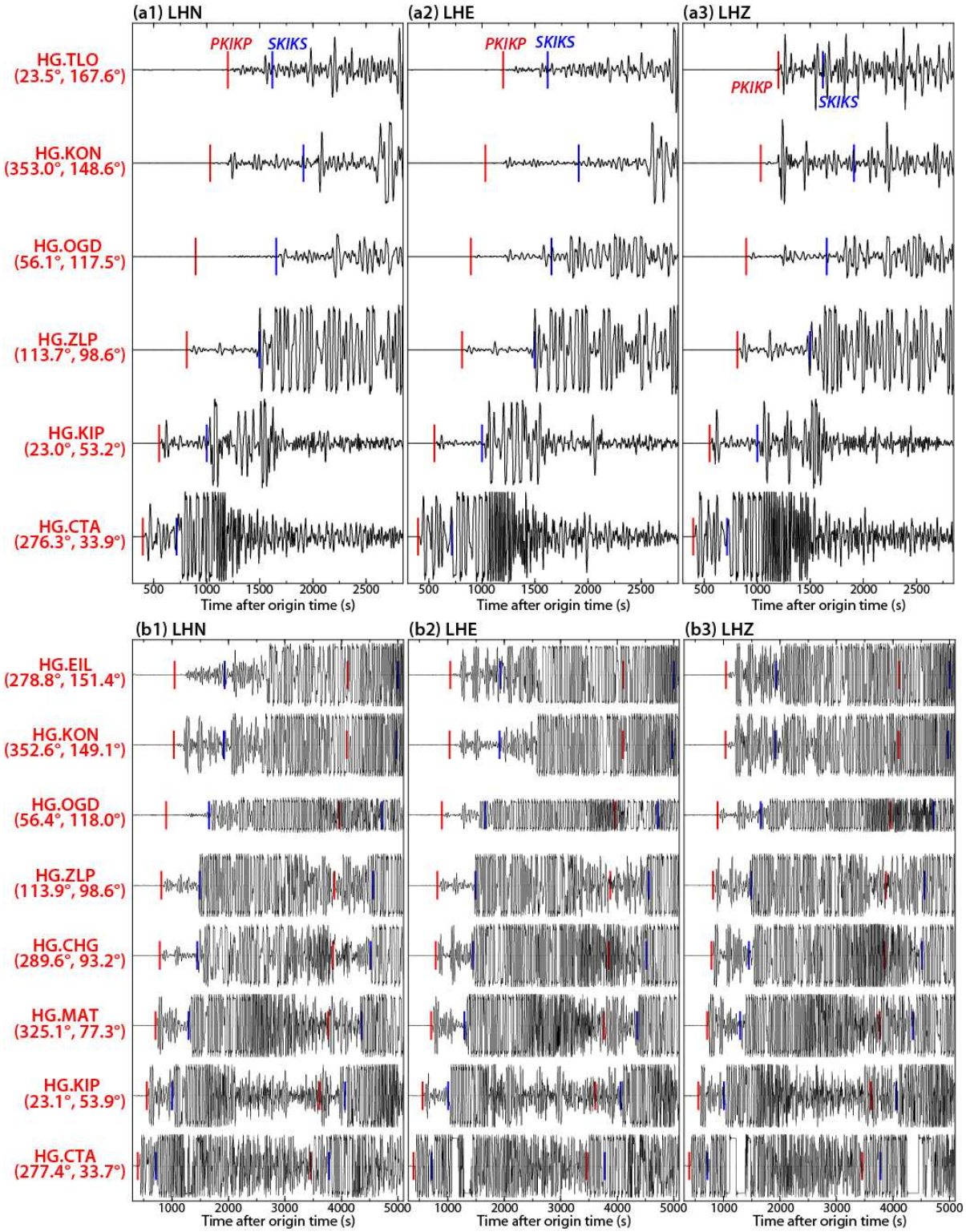

Figure S14. Raw seismic waveforms of the 1976 major earthquakes at stations in the HG network. (a1-a3) raw seismic waveforms of the 1976 M_W 7.3 earthquake, and (b1-b3) for the 1976 M_W 7.8 and M_W 7.9 earthquakes. The red and blue bars are the theoretical arrival times of the *P* and *S* phases predicted by the IASP91 model. The *PKIKP* and *SKIKS* phases are labeled for the station HG.TLO. The polarity of the LHZ component of OGD data is reversed.

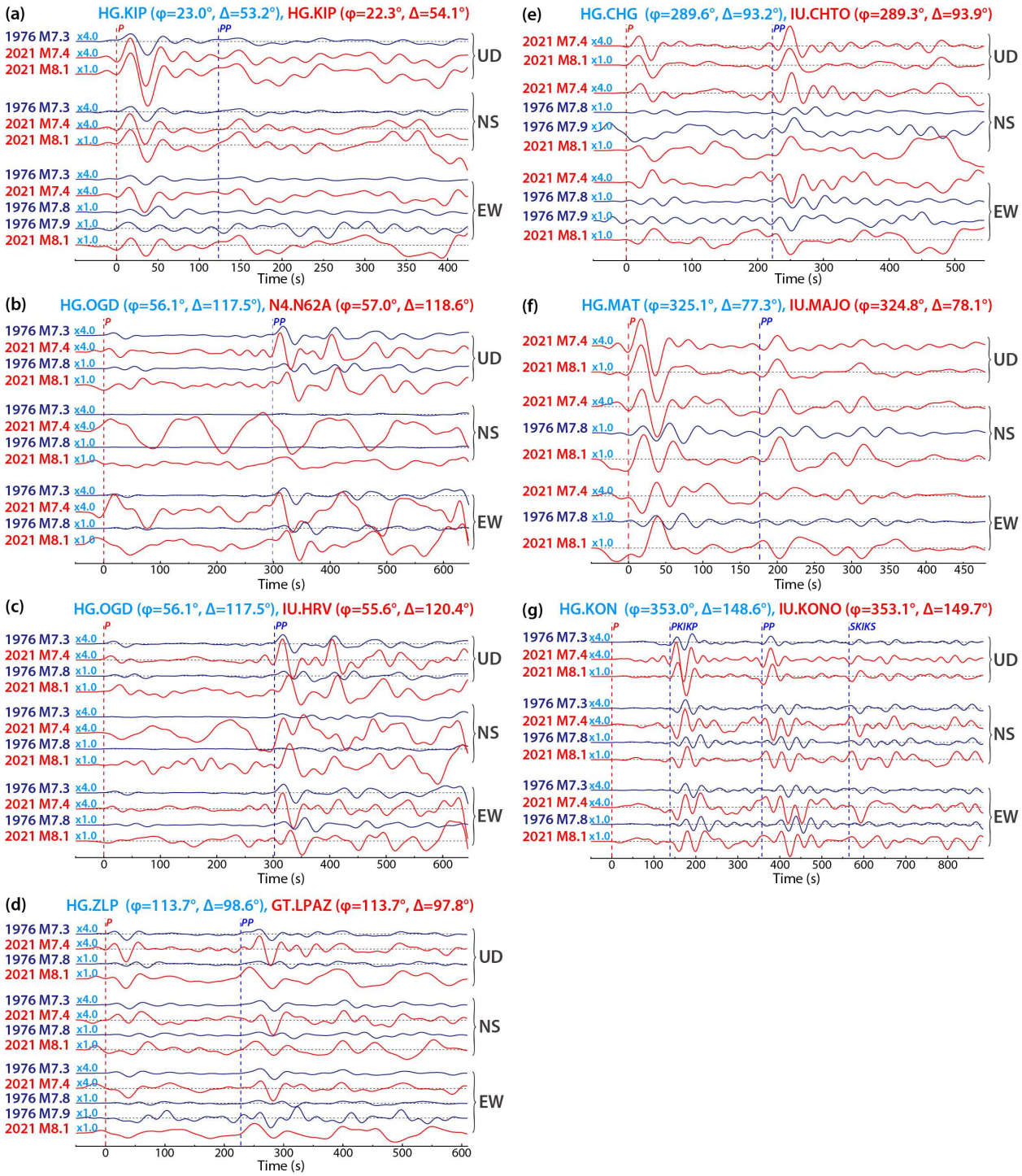

Figure S15. Comparisons of seismic waveforms for the 1976 and 2021 major earthquakes at stations in the HG network. Three-component displacement records are filtered in the period band of 30-150 s. Each component in every panel shares a common scale, with the amplitude for the 1976 M_W 7.3 and 2021 M_W 7.4 multiplied by 4. Data are aligned with *P* arrivals. The relative arrival times for *PKIKP*, *PP*, and *SKIKS* phases predicted by the IASP91 model are labeled.

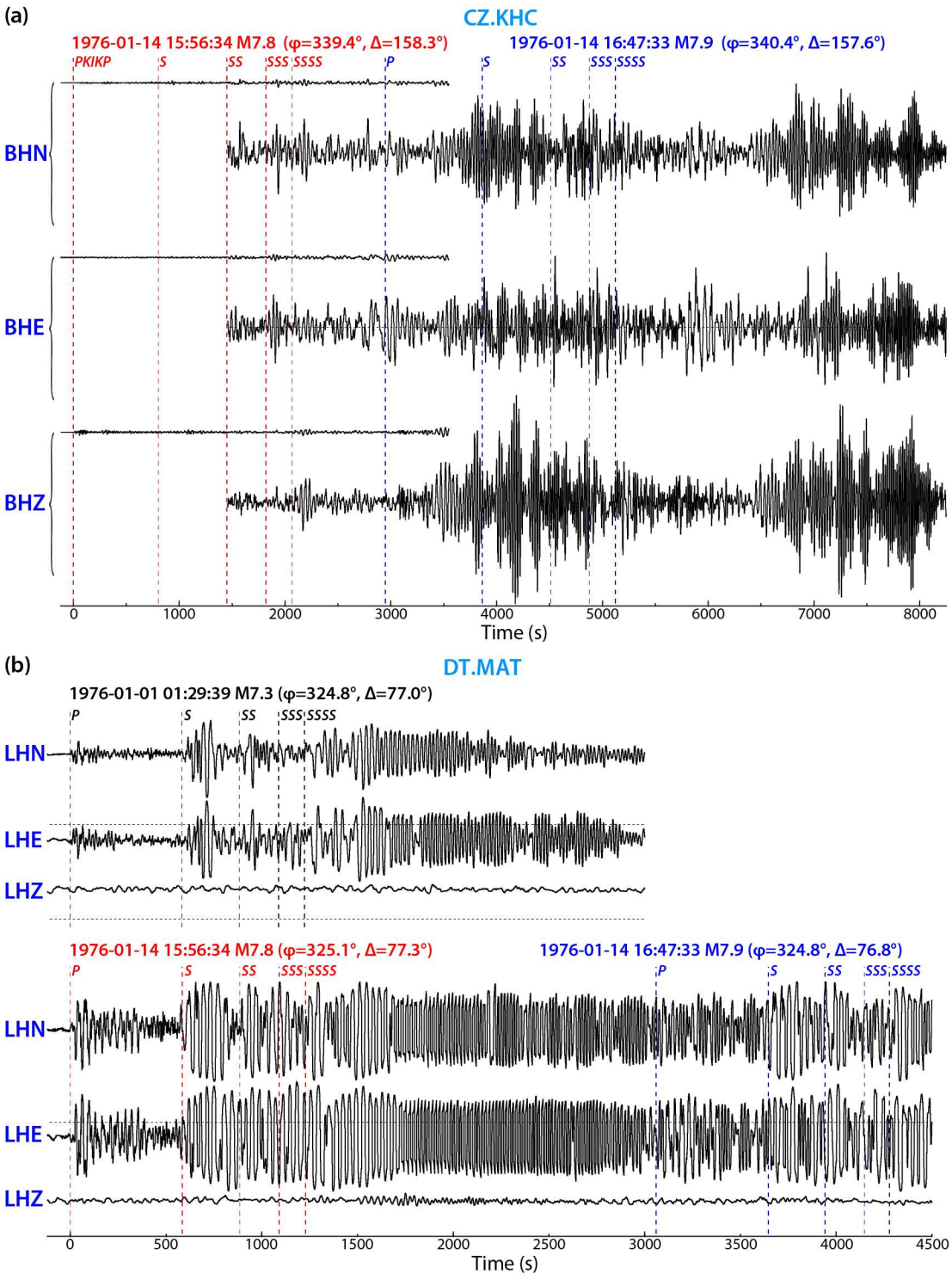

Figure S16. Problematic Raw seismic waveforms of the three 1976 major earthquakes at stations (a) CZ.KHC and (b) DT.MAT. Data are aligned on *P* or *PKIKP* arrivals. The relative arrival times for *S*, *SS*, *SSS*, and *SSSS* phases predicted by the IASP91 model are labeled. For CZ.KHC, each component includes two segments in the overlapping part but different amplitudes. Data at station MAT have severe noise and lack instrumental response files.

Table S1. Information for events between M_W 7.4 and M_W 8.1 events from the ISC catalog

Event	Origin Time	Longitude (°)	Latitude (°)	Depth (km)	Mag (mb)	Author
E00	2021-03-04T17:41:23.89	-177.814	-29.689	40.2	6.6	ISC
E01	2021-03-04T17:51:10.28	-177.426	-29.738	10.0	5.0	ISC
E02	2021-03-04T17:56:03.78	-177.024	-29.757	24.0	4.7	ISC
E03	2021-03-04T17:57:56.16	-177.079	-29.833	10.0	4.8	ISC
E04	2021-03-04T17:59:12.57	-177.154	-29.862	24.0	5.6	ISC
E05	2021-03-04T18:07:49.09	-177.179	-29.796	24.0	5.4	ISC
E06	2021-03-04T18:14:58.25	-177.175	-29.471	31.0	4.3	ISC
E07	2021-03-04T18:18:57.69	-177.026	-29.648	0.0	3.5	IDC
E08	2021-03-04T18:20:28.68	-177.546	-28.547	0.0	4.2	IDC
E09	2021-03-04T18:24:10.59	-177.054	-29.547	31.0	4.3	ISC
E10	2021-03-04T18:33:58.55	-177.515	-29.870	35.0	4.4	ISC
E11	2021-03-04T18:38:33.15	-177.472	-28.496	0.0	3.7	IDC
E12	2021-03-04T18:39:12.94	-176.954	-29.760	24.0	4.2	ISC
E13	2021-03-04T18:42:06.15	-177.391	-28.798	10.0	4.2	ISC
E14	2021-03-04T18:42:48.11	-177.082	-30.416	24.0	4.5	ISC
E15	2021-03-04T18:52:47.21	-177.452	-29.726	52.0	4.8	ISC
E16	2021-03-04T18:55:51.74	-177.329	-29.421	52.0	4.4	ISC
E17	2021-03-04T19:00:39.19	-177.809	-28.609	10.0	4.6	ISC
E18	2021-03-04T19:02:32.35	-177.163	-28.820	36.0	4.3	ISC
E19	2021-03-04T19:06:34.53	-177.231	-29.744	10.0	4.9	ISC
E20	2021-03-04T19:13:11.23	-177.168	-29.771	24.0	5.2	ISC
E21	2021-03-04T19:15:30.43	-177.923	-28.578	10.0	4.8	ISC
E22	2021-03-04T19:20:29.05	-177.051	-29.744	31.0	4.8	ISC
E23	2021-03-04T19:28:34.63	-177.091	-29.442	20.1	6.9	ISC

Note: 1) E00 and E23 are the M_W 7.4 foreshock and M_W 8.1 mainshock, respectively.

2) E01, E03, E04, E05, E09, E10, E13, E14, E15, E16, E17, E19, E20, E21, E22 are also listed in the USGS-NEIC catalog but with some variations in origin time and location (see Figure 6).

Table S2. Summary of digital seismic data available for the three 1976 major earthquakes

Corresponding stations with available data for the 2021 earthquakes are nearest to the 1976 stations. Highlighted stations are used in this study. LH: long period, high gain seismometer. BH: broadband, high gain seismometer. HH: high broadband, high gain seismometer. VH: very long period, high gain seismometer. SH: short period, high gain seismometer. LL: long period, low gain seismometer. LM: long period, mass position seismometer. SM: short period, mass position seismometer. EH: extremely short period, high gain seismometer.

#	STA (1976)	Network (1976)	Lat (˚N) Lon (˚E)	Channels (1976)	SAT (2021)	Network (2021)	Lat (˚N) Lon (˚E)	Channels (2021)	Detailed information
1	ANMO	SR	34.9 -106.5	LH, SHZ	ANMO	IU	34.9 -106.5	LH, BH, HH, VH	Data are not clipped for the 1976 M7.3 event. Body waves are not clipped in the 1976 M7.8 and M7.9 data.
2	GUMO	SR	13.6 144.9	LH, SHZ	GUMO	IU	13.6 144.9	LH, BH, HH, VH	Data are not clipped for the 1976 M7.3 event. Body waves are mostly not clipped in the 1976 M7.8 and M7.9 events, with S waves slightly clipped in the 1976 M7.9 data.
3	MAIO	SR	36.3 59.5	LH, SHZ	DZET	CK	38.8 68.8	HH	The nearest stations for 2021 events are DZET (~868 km) and KBL (~886 km).
					KBL	IU	34.5 69.0		
4	CHG	HG	18.8 99.0	LH	CHTO	IU	18.8 98.9	BH, HH, LH, VH	No data for the 1976 M7.3 event. LHZ component of 1976 M7.9 data and LHZ of M7.8 data are clipped. P waves of LHN and LHE components are not clipped for the M7.8 and M7.9 events.
5	CTA	HG	-20.1 146.3	LH	CTAO	IU	-20.1 146.2	BH, HH, LH, VH	The 1976 events data are clipped on all components.
6	EIL	HG	29.5 35.0	LH	EIL	GE	29.7 35.0	BH, HH, LH, VH, SH	No data for the 1976 M7.3 event. All components of the 1976 M7.9 data and LHZ of M7.8 data are clipped. For the M7.8 event, the LHE component is clipped at the PP phase, the LHN component is clipped after the SS phase, LHZ component is clipped at PKP.
7	KIP	HG	21.4 -158.0	LH	KIP	IU	21.4 -158.0	BH, HH, LH, VH	For the 1976 M7.3 data, P waves of LHN and LHE are not clipped, and body waves of LHZ are not clipped. LHN and LHZ are clipped for the M7.8 and M7.9 events. *P* waves of LHE are not clipped for the M7.8 and M7.9 events.
8	KON	HG	59.6 9.6	LH	KONO	IU	59.6 9.6	BH, HH, LH, VH	All components of the 1976 M7.9 data are clipped. The M7.3 data is clipped at *SS* phase. For the M7.8 event, LHZ is clipped at the *PKP* phase, LHN at the S_{diff} phase, and LHE at *SS* phase.
9	MAT	HG	36.5 138.2	LH	MAJO	IU	36.5 138.2	BH, HH, LH, VH	No data for the M7.3 event. Data are clipped on all components of the M7.9 event. P waves of LHN and

									LHE components are not clipped for the M7.8 event, LHZ component of the M7.8 event is clipped.
10	OGD	HG	41.1 -74.6	LH	N62A	N4	40.9 -73.5	LH	The nearest station (N62A) for 2021 events is ~96 km away. P wave is not clipped for the M7.3 and M7.8 events. All components are clipped for the M7.9 event. Data of 2021 events are of bad quality. HRV (297 km) of IU network is of better quality than N62A.
					IU	HRV	42.5 -71.6	LH, BH	
11	TLO	HG	39.9 -4.0	LH	PAB	IU	39.5 -4.3	BH, HH, LH, VH	No data for the 1976 M7.8 and M7.9 events. The M7.3 data is clipped at the SS phase.
12	ZLP	HG	-16.3 -68.1	LH	LPAZ	GT	-16.3 -68.1	BH, SHZ	The 1976 M7.3 and M7.8 data are clipped at S waves. LHN and LHZ components of the 1976 M7.9 are clipped, P wave of LHE is not clipped.
13	MAT	DT	36.5 138.2	LH, LM, LL, SH, SM	MAJO	IU	36.5 138.2	BH, HH, LH, VH	No instrumental response files for all data. Poor data quality.
14	KHC	CZ	49.1 13.6	BH	KHC	CZ	49.1 13.6	BH, EH, HH, LH, SH	Something corrupted the amplitude of KHC data.

208